Mechanical Systems and Signal Processing 201 (2023) 110652

Contents lists available at ScienceDirect

Mechanical Systems and Signal Processing

journal homepage: www.elsevier.com/locate/ymssp

Experimental assessment of Bayesian and mode matching approaches for parametric identification of bolted connections

Mariusz Ostrowski *, Grzegorz Mikułowski, Bartlomiej Blachowski, Łukasz Jankowski

Institute of Fundamental Technological Research, Polish Academy of Sciences, Pawińskiego 5B, 02-106 Warsaw, Poland

ARTICLE INFO

Communicated by J.E. Mottershead

Keywords:
Mode matching
Bayesian approach
Parametric identification
Uncertain bolted connections
Parameter uncertainty
Convergence

ABSTRACT

This paper investigates the problem of parametric identification of highly uncertain bolted connections. The unknown parameters representing stiffness of the connections are estimated using two commonly accepted methods: (1) the traditional mode matching approach and (2) a probabilistic Bayesian framework based on the maximum a posteriori (MAP) formulation. Additionally, the uncertainties of the unknown parameters are also estimated and compared for both methods. A numerical example and a real lab-scale frame structure with highly uncertain bolted connections were used in the tests. In the experimental case, the system eigenvalues (squares of the natural frequencies) and the mode shapes measured in a broad frequency range were employed. The measured mode shapes were strongly disturbed by assembly discrepancies of the bolted connections. Finally, both methods were compared in terms of computational efficiency on a large-scale FE model (31,848 degrees of freedom). Despite the sophistication of the Bayesian approach in treating the trade-off between measurement errors and expected modeling errors, the results indicate that the two tested methods yield similar values for the unknown parameters. The Bayesian approach requires numerical regularization to calculate the parameter covariance matrix, which may decrease its reliability. In contrast, the mode matching method avoids such numerical difficulties. Furthermore, the Bayesian approach requires a much larger number of iterations and a careful selection of the weighting parameters.

1. Introduction

Modern computer technologies allow for development and use of sophisticated finite element (FE) models. However, in many engineering applications, it is still difficult to reliably replicate the physical behavior of the system using its FE model. In such cases, the model needs to be modified using experimentally measured data, and the respective process is called *model updating* [1,2]. Usually, model updating has two main purposes: (1) identification of the unknown system parameters and (2) obtaining a model that correctly reproduces the behavior of the physical system [3]. In both cases, the model updating procedure is prone to measurement noise and modeling errors. Additionally, the identification problem may be ill-conditioned. Thus, model updating methods should incorporate some knowledge about the involved errors, especially in damage assessment applications [4]. In practical problems, it is usually assumed that the errors between the measurement data and the model output (including measurement noise and modeling error) are spatially and temporally uncorrelated. However, this is not always true, e.g., if sensors are distributed very densely on the structure. Such correlations can affect the estimates of the unknown parameters and their uncertainties, as shown by Simeon et al. [5].

* Corresponding author.
E-mail addresses: mostr@ippt.pan.pl (M. Ostrowski), gmikulow@ippt.pan.pl (G. Mikułowski), bblach@ippt.pan.pl (B. Blachowski), ljank@ippt.pan.pl (Ł. Jankowski).

https://doi.org/10.1016/j.ymssp.2023.110652
Received 20 February 2023; Received in revised form 24 July 2023; Accepted 30 July 2023

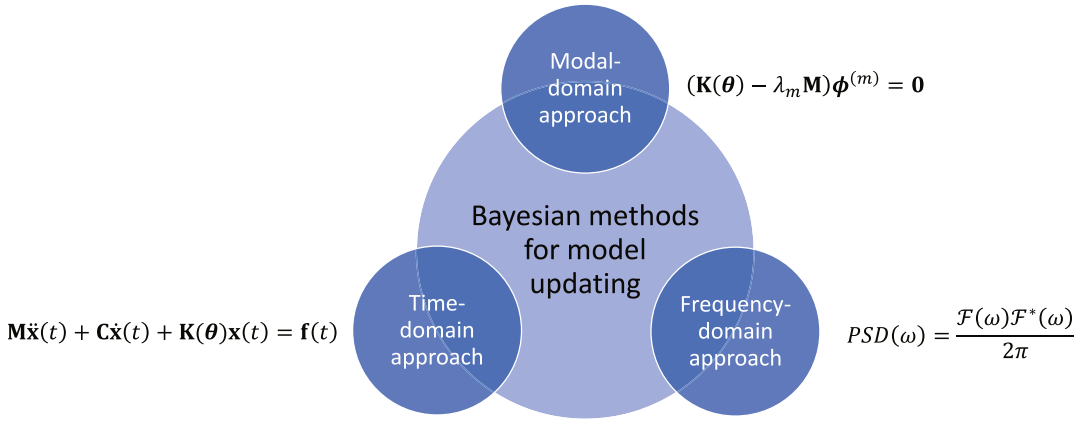

Fig. 1. Categorization of the Bayesian methods for model updating according to the processed measurement data.

The classical model updating methods can be categorized according to the way they obtain the updated model [1], that is, into: (1) direct methods and (2) iterative methods. Direct methods have important disadvantages. They usually strive to exactly reproduce the measurement data, which includes the measurement noise. Moreover, they often require either model reduction or extrapolation of the measurement data from measurement locations to the configuration space of the model. As a result, the updated model might be meaningless in terms of its physical properties. An example of a direct method was proposed by Yang and Chen [6]. The method searches for such increments of the mass and stiffness matrices that compensate for the error between the numerical and the measured modal data.

In contrast to the direct methods that update raw structural matrices, the iterative methods operate at a higher level and update the parameters of a certain parametric structural model. Such an approach does not usually allow for an exact reproduction of the system behavior, but it is free from many disadvantages of the direct methods. Many iterative methods for model updating use modal data. One of the classical approaches is based on modal sensitivity to certain predefined parameters of the structure, as proposed by Friswell and Mottershead [7]. The objective function to be minimized is the norm of the error between the numerical and the experimental modal data. Such an approach requires mode matching: the experimentally obtained modes need to be matched with the numerical modes in order to calculate the objective function. It is thus called the *mode matching method* in the further parts of this paper.

The categorization into iterative and direct methods is not always clear, as some methods are formally iterative but retain the properties of direct methods. The iterative method proposed by Sarmadi et al. [8] fits the model to measurement data using the direct formulation discussed in [6]. An iterative scheme is used to solve the equations augmented with a quadratic term to enhance the accuracy. Like direct methods, it searches for entire matrices instead of predefined parameters. Another iterative method was proposed by Yuan and Liu [9], and it also uses a matrix formulation instead of local model parameters. The model is updated by minimizing the Frobenius norm of the difference between the initial (before updating) and the actual stiffness and damping matrices, while keeping the eigenproblem satisfied for the measured modal data.

An example of a classical model updating method is the minimum variance method proposed by Collins et al. [10,11], which finds the values of model parameters that provide the minimum variances. Similarly to the Bayesian methods, the approach is statistical in nature. The *Bayesian methods* for model updating are usually formulated in a rigorous probabilistic framework and account for both measurement and modeling errors [12]. They provide a powerful tool for parametric identification, and thanks to the probabilistic formulation, they also allow for the calculation of the uncertainties of the identified parameters. Mode matching methods can also be formulated probabilistically and classified as Bayesian methods when an additional regularization term is introduced based on prior knowledge about the unknown parameters [13–15]. Regularization typically reduces the variance of the identified parameters, but at the expense of increased bias error. This bias can be mitigated by incorporating prior knowledge about the estimated parameters through constraints imposed on the objective function. Ostrowski et al. [16] demonstrated that mode matching with the constraint that stiffness parameters can only decrease from their initial values (for damage detection purposes) significantly outperforms methods that employ regularization based on the truncated singular value decomposition (TSVD). However, despite the effectiveness of such constrained optimization, it may not always be applied, as prior knowledge about possible constraints is often limited.

The Bayesian methods for model updating can be categorized according to the type of data they process (Fig. 1) [3]:

- Bayesian frequency-domain approaches that utilize the properties of the power spectral density function and use frequency-domain measurement data;
- Bayesian time-domain approaches that use time histories of the system output;
- Bayesian modal-domain approaches that use measured natural frequencies and mode shapes.

Frequency-domain approaches tend to be less computationally demanding than their time-domain counterparts. A computationally effective Bayesian spectral density method was proposed by Zhang et al. [17]. Frequency-domain approaches are suitable

for both linear and nonlinear systems, while time-domain approaches are typically appropriate for linear systems only. They also introduce fewer approximations while processing the measurement data. Furthermore, time-domain approaches can be applied to nonstationary data, whereas frequency-domain approaches can usually be used only with stationary processes. Sedehi et al. [18] proposed an interesting time-domain Bayesian approach that leverages the hierarchical structure of the probabilistic model to accurately estimate the uncertainty propagation.

An advantage of Bayesian modal-domain methods is that the updating algorithm does not use large amounts of data. The modal data need to be extracted beforehand from the available measurement data. It can be performed using such classical methods as the stochastic subspace identification [19,20]. Bayesian methods for identification of modal parameters are also available, such as the autoregressive model proposed by Yang and Lam [21]. A modal-domain approach for the calculation of the posterior probability density function for bolt loosening in large-scale structures was proposed by Yin et al. [22]. Periodically supported structures with bolted-flange joints were considered and divided into repetitive cells to reduce the computational effort, and Bayesian model class selection was employed to obtain a representative model of the joints.

Model updating based on balancing the eigenproblem equation avoids the mode matching problem, but it introduces numerical difficulties that often corrupt the results. The Bayesian formulation of the maximum a posteriori (MAP) estimate allows the optimization objectives to be augmented with regularization terms that balance the eigenproblem equation [23,24]. This reduces numerical difficulties while still avoiding the mode matching problem.

In addition to measurement and modeling errors, a significant problem in model updating is the detectability and proper sensor placement. The detectability depends on system configuration: if a structural element does not take part in the response (is not strained), then its stiffness cannot be identified [25]. Blachowski [26] discussed the problem of selecting appropriate sensor locations and used a modal sensitivity matrix to determine damage-sensitive locations. Exciting more vibration modes was found to be usually more effective than employing a greater number of sensors, which agrees with the observation on the detectability of stiffness changes: the more modes are excited and measured, the greater the chance to involve all structural members in the response. In practice, large-scale FE models are often used, which makes sensor placement a computationally demanding combinatorial problem. An effective technique in such cases is convex relaxation, which represents the discrete problem with its continuous counterpart [27].

Measured modal data can be insufficient to detect some types of damage, such as the loss of preload in bolted connections. Biswal et al. investigated this problem and proposed a model updating strategy that employs time-domain displacement response of the structure [28]. Due to local nonlinear effects, the model of the bolted connection had to be modified by adding a viscous damper. Many researches focus on identifying bolted connections with only a single bolt, whereas civil structures or industrial systems commonly involve multiple-bolt connections. Wang et al. proposed a methodology using a genetic algorithm to monitor connections including multiple bolts [29]. Szopa et al. investigated a truss mast structure with 152 bolted connections [30]. A multi-criteria optimization problem was formulated and solved to obtain Pareto-optimal solutions. However, the bolted connections were not parameterized independently of each other, and they shared the same parameters. The behavior of bolted connections depends on local effects, such as the distribution of contact pressure, which can affect the equivalent stiffness of the connection [31]. Thus, their behavior can be sensitive to assembly discrepancies and operational wear. To the authors' knowledge, there is a limited number of publications dedicated to structures where all bolted connections are highly uncertain, i.e., their stiffness parameters are strongly disturbed due to assembly discrepancies or operational wear. Such discrepancies can affect modal data, especially higher-order mode shapes that become disturbed.

This paper compares and evaluates two widely accepted methods for model updating: (1) mode matching method, and (2) a probabilistic Bayesian framework for maximum a posteriori (MAP) estimation without mode matching. They are compared using numerical data with known exact parameter values, as well as a lab frame structure with 16 independently parameterized, highly uncertain bolted connections. Section 2 describes the class of models considered, provides background on model updating based on mode matching and the Bayesian approach. It includes also an illustrative numerical example. In Section 3, the lab-scale frame with 16 highly uncertain bolted connections is described. The FE model of the frame and two parameterizations of the connections are introduced. The section ends with a description of the measured modal data and their statistical uncertainty metrics. Section 4 provides an extensive comparison of the two tested methods in terms of the identified parameters, their uncertainties, and error metrics that quantify the differences between the FE model and the real frame. Section 5 compares the computational efficiency of both methods using a large-scale FE model, simulated measurement data, and known exact parameter values. Conclusions are summarized in Section 6.

2. Parametric identification of bolted connections

2.1. Model and parameterization of a bolted connection

A class $\mathcal{C}$ of structural models $(\mathbf{M}, \mathbf{K}(\boldsymbol{\theta}))$ is considered, where $\mathbf{M}$, $\mathbf{K} \in \mathbb{R}^{N_\mathrm{d} \times N_\mathrm{d}}$ are the mass and stiffness matrices, respectively, N_d is the number of degrees of freedom (DOFs), and $\boldsymbol{\theta} \in \mathbb{R}_+^{N_\theta}$ is the vector of N_θ unknown parameters of the model. The mass matrix, $\mathbf{M}$, is assumed to be known. The stiffness matrix, $\mathbf{K}(\boldsymbol{\theta})$, is defined as follows:

$$\mathbf{K}(\boldsymbol{\theta}) = \mathbf{K}_0 + \sum_{l=1}^{N_\theta} \theta_l \mathbf{K}_l, \tag{1}$$

where $\mathbf{K}_0$ represents the well-known part of the structure, which can be estimated sufficiently accurately, e.g., based on the technical documentation. The components $\mathbf{K}_l$ are associated with uncertain parts of the structure, such as bolted connections, whose stiffness remains unknown.

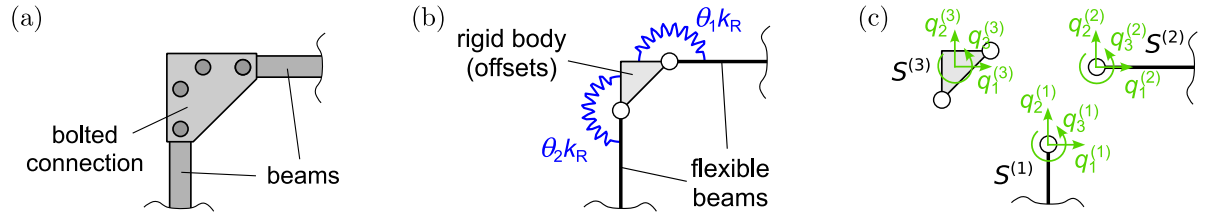

Fig. 2. Bolted connection: (a) schematic representation; (b) parameterization with two parameters, θ_1 and θ_2, corresponding to the rotational stiffness of the nominal value k_R; (c) division into three substructures: beams $S^{(1)}$ and $S^{(2)}$, and the rigid body $S^{(3)}$.

An example of a bolted connection is shown in Fig. 2a. Two beams are connected via a coupler. Due to relatively small size and high stiffness, the coupler is represented by a rigid body. The bolted connections between the coupler and the beams are modeled as springs k_R between the involved rotational DOFs, as shown in Fig. 2b. Hence, for the lth connection,

$$\mathbf{K}_l = k_R \boldsymbol{\ell}_l \boldsymbol{\ell}_l^T, \tag{2}$$

where $\boldsymbol{\ell}_l = \begin{bmatrix} \cdots & 0 & 1 & 0 & \cdots & 0 & -1 & 0 & \cdots \end{bmatrix}^T \in \mathbb{R}^{N_d}$ is a column vector of the appropriate dimension that selects the rotational DOFs involved in the lth bolted connection. The entire connection is assembled as shown in Fig. 2c. The dynamics of the substructures $S^{(i)}$, $i = 1, 2, 3$, is described by Eq. (3) [32].

$$\begin{cases} \widetilde{\mathbf{M}} \underbrace{\mathbf{L}\ddot{\mathbf{q}}(t)}_{\ddot{\widetilde{\mathbf{q}}}(t)} + \widetilde{\mathbf{K}} \underbrace{\mathbf{L}\mathbf{q}(t)}_{\widetilde{\mathbf{q}}(t)} = \widetilde{\mathbf{f}}(t) + \mathbf{g}(t), \\ \mathbf{B}\mathbf{q}(t) = \mathbf{0} \\ \mathbf{L}^T \mathbf{g}(t) = \mathbf{0}, \end{cases} \tag{3}$$

where

$$\widetilde{\mathbf{M}} = \begin{bmatrix} \widetilde{\mathbf{M}}^{(1)} & \mathbf{0} & \mathbf{0} \\ \mathbf{0} & \widetilde{\mathbf{M}}^{(2)} & \mathbf{0} \\ \mathbf{0} & \mathbf{0} & \widetilde{\mathbf{M}}^{(3)} \end{bmatrix}, \quad \widetilde{\mathbf{K}} = \begin{bmatrix} \widetilde{\mathbf{K}}^{(1)} & \mathbf{0} & \mathbf{0} \\ \mathbf{0} & \widetilde{\mathbf{K}}^{(2)} & \mathbf{0} \\ \mathbf{0} & \mathbf{0} & \widetilde{\mathbf{K}}^{(3)} \end{bmatrix}$$

denote, respectively, the mass and stiffness matrices prior to system assembly, $\widetilde{\mathbf{q}}(t)$ is the corresponding displacement vector, $\mathbf{L}$ represents the transformation matrix (or assembly matrix), $\mathbf{q}(t)$ is the vector of unique displacements, $\widetilde{\mathbf{f}}(t)$ represents the vector of external forces, the vector $\mathbf{g}(t)$ collects the coupling forces on the interfaces between the substructures $S^{(i)}$, and $\mathbf{B}$ is signed Boolean matrix that selects DOFs involved in the interfaces between substructers $S^{(i)}$.

The substructure $S^{(3)}$ represents a rigid body, and its motion is represented by three DOFs at its center of gravity. The displacements of $S^{(3)}$ are expressed in terms of the displacements at its interfaces, as shown in Fig. 2c. Due to such geometrical dependencies, the assembly matrix $\mathbf{L}$ is not purely Boolean [32]. According to the primal assembly formulation, Eq. (3) is left-multiplied by $\mathbf{L}^T$, which yields the following equation of motion in unique coordinates:

$$\mathbf{M}\ddot{\mathbf{q}}(t) + \mathbf{K}_0 \mathbf{q}(t) = \mathbf{f}(t), \tag{4}$$

where $\mathbf{M} = \mathbf{L}^T \widetilde{\mathbf{M}} \mathbf{L}$, $\mathbf{K}_0 = \mathbf{L}^T \widetilde{\mathbf{K}} \mathbf{L}$, and $\mathbf{f}(t) = \mathbf{L}^T \widetilde{\mathbf{f}}(t)$. After the primal assembly of the structure shown in Fig. 2c, the rotational stiffnesses defined in Eq. (2) are added to $\mathbf{K}_0$ according to Equation (1), and the system shown in Fig. 2b is finally obtained.

2.2. Mode matching for parameter estimation

The classical model updating framework based on modal sensitivity is discussed here. The model updating process amounts to solving the optimization problem (P_1), defined as follows:

$$(P_1) \qquad \begin{aligned} &\text{find} && \boldsymbol{\theta} \\ &\text{to minimize} && \varepsilon(\boldsymbol{\theta}), \end{aligned}$$

where $\varepsilon(\boldsymbol{\theta})$ is the weighted square error between the measured and numerical modal data, which is an error metric widely used for model updating [1,7,13–16,26]:

$$\varepsilon(\boldsymbol{\theta}) = \mathbf{e}^T(\boldsymbol{\theta}) \mathbf{W} \mathbf{e}(\boldsymbol{\theta}). \tag{5}$$

The error vector $\mathbf{e}(\boldsymbol{\theta})$ involves both eigenvalues and mode shapes, and it is defined as follows:

$$\mathbf{e}(\boldsymbol{\theta}) = \begin{bmatrix} \widehat{\boldsymbol{\lambda}} \\ \widehat{\boldsymbol{\psi}} \end{bmatrix} - \begin{bmatrix} \boldsymbol{\lambda}_{num}(\boldsymbol{\theta}) \\ \mathbf{L}_o \boldsymbol{\phi}_{num}(\boldsymbol{\theta}) \end{bmatrix}, \tag{6}$$

where the vectors $\widehat{\lambda} \in \mathbb{R}_{+}^{N_m}$ and $\widehat{\boldsymbol{\psi}} = \left[\widehat{\boldsymbol{\psi}}^{(1)\mathrm{T}} \quad \widehat{\boldsymbol{\psi}}^{(2)\mathrm{T}} \quad \cdots \quad \widehat{\boldsymbol{\psi}}^{(N_m)\mathrm{T}}\right]^{\mathrm{T}} \in \mathbb{R}^{N_m N_\mathrm{o}}$ collect the N_m measured eigenvalues and mode shapes, respectively, and N_o denotes the number of sensor locations. Similarly, $\lambda_{\mathrm{num}}(\boldsymbol{\theta})$ and $\boldsymbol{\phi}_{\mathrm{num}}(\boldsymbol{\theta})$ collect the numerical eigenvalues $\lambda_m^{\mathrm{num}}(\boldsymbol{\theta})$ and the properly scaled numerical mode shapes $c_m \boldsymbol{\phi}_{\mathrm{num}}^{(m)}(\boldsymbol{\theta}) \in \mathbb{R}^{N_\mathrm{d}}$ obtained from the FE model $(\mathbf{M}, \mathbf{K}(\boldsymbol{\theta}))$. The modal scale factor c_m is defined as:

$$c_m = \frac{\widehat{\boldsymbol{\psi}}^{(m)\mathrm{T}} \mathbf{D} \boldsymbol{\phi}_{\mathrm{num}}^{(m)}}{\left\| \mathbf{D} \boldsymbol{\phi}_{\mathrm{num}}^{(m)} \right\|^2}. \tag{7}$$

The Boolean matrix $\mathbf{D} \in \{0,1\}^{N_\mathrm{o} \times N_\mathrm{d}}$ selects the measured DOFs, and $\mathbf{L}_\mathrm{o}$ in Eq. (6) is a block-diagonal matrix composed of $\mathbf{D}$. The weighting matrix $\mathbf{W}$ in Eq. (5) is usually reciprocal to the measurement covariance matrix $\boldsymbol{\Sigma}_\mathrm{M}$, whose entries correspond to the elements of $\mathbf{e}(\boldsymbol{\theta})$,

$$\mathbf{W} = \boldsymbol{\Sigma}_\mathrm{M}^{-1}. \tag{8}$$

Alternatively, if $\boldsymbol{\Sigma}_\mathrm{M}$ is not available, then the weighting matrix can be calculated as follows:

$$\mathbf{W} = \mathrm{diag}\left(\left[\widehat{\lambda}_1^{-2}, \quad \widehat{\lambda}_2^{-2}, \quad \cdots \quad \widehat{\lambda}_{N_m}^{-2}, \quad \frac{w_\psi}{\frac{1}{N_\mathrm{o}} \left\| \widehat{\boldsymbol{\psi}}^{(1)} \right\|^2} \mathbf{1}_\mathrm{o}^{\mathrm{T}}, \quad \frac{w_\psi}{\frac{1}{N_\mathrm{o}} \left\| \widehat{\boldsymbol{\psi}}^{(2)} \right\|^2} \mathbf{1}_\mathrm{o}^{\mathrm{T}}, \quad \cdots \quad \frac{w_\psi}{\frac{1}{N_\mathrm{o}} \left\| \widehat{\boldsymbol{\psi}}^{(N_m)} \right\|^2} \mathbf{1}_\mathrm{o}^{\mathrm{T}} \right]^{\mathrm{T}} \right), \tag{9}$$

where w_ψ is a weight that quantifies the lower measurement accuracy of the mode shapes in comparison to the natural frequencies, and $\mathbf{1}_\mathrm{o}$ is the N_o-long vector of ones.

From Eq. (5) it is evident that the mode matching method searches for the model $(\mathbf{M}, \mathbf{K}(\boldsymbol{\theta}))$ that best reproduces the measured output of the system, as expressed in terms of its measured modal parameters.

2.3. Bayesian approach for parameter estimation

The Bayesian framework proposed by Yuen et al. [3,23] does not insist that the vibration modes $\boldsymbol{\phi}^{(m)} \in \mathbb{R}^{N_\mathrm{d}}$ and eigenvalues $\lambda_m \in \mathbb{R}_{+}$ of the identified system satisfy the eigenvalue problem for the structural model $(\mathbf{M}, \mathbf{K}(\boldsymbol{\theta}))$. Instead, the framework explicitly includes the insight that both measurement data and mathematical model of the structure are subject to certain errors. Accordingly, the measurement error $\mathbf{e}_\mathrm{M}$ is introduced as follows:

$$\mathbf{e}_\mathrm{M}(\lambda, \boldsymbol{\phi}) = \begin{bmatrix} \widehat{\lambda} \\ \widehat{\boldsymbol{\psi}} \end{bmatrix} - \begin{bmatrix} \lambda \\ \mathbf{L}_\mathrm{o} \boldsymbol{\phi} \end{bmatrix}, \tag{10}$$

where $\lambda \in \mathbb{R}^{N_m}$ and $\boldsymbol{\phi} = \left[\boldsymbol{\phi}^{(1)\mathrm{T}} \quad \boldsymbol{\phi}^{(2)\mathrm{T}} \quad \cdots \quad \boldsymbol{\phi}^{(N_m)\mathrm{T}}\right]^{\mathrm{T}} \in \mathbb{R}^{N_m N_\mathrm{d}}$ collect the system eigenvalues and mode shapes that remain unknown. They are treated as random variables. For a FE model of class $\mathcal{C}$, the modeling error $\mathbf{e}_\mathcal{C}(\lambda, \boldsymbol{\phi}, \boldsymbol{\theta})$ is introduced as follows:

$$\mathbf{e}_\mathcal{C}(\lambda, \boldsymbol{\phi}, \boldsymbol{\theta}) = \begin{bmatrix} \left(\mathbf{K}(\boldsymbol{\theta}) - \lambda_1 \mathbf{M}\right) \boldsymbol{\phi}^{(1)} \\ \vdots \\ \left(\mathbf{K}(\boldsymbol{\theta}) - \lambda_{N_m} \mathbf{M}\right) \boldsymbol{\phi}^{(N_m)} \end{bmatrix}. \tag{11}$$

Additionally, a quantity $\mathbf{e}_\theta$ is introduced:

$$\mathbf{e}_\theta(\boldsymbol{\theta}) = \boldsymbol{\theta} - \boldsymbol{\theta}_0, \tag{12}$$

where $\boldsymbol{\theta}_0$ is the vector of nominal values of the unknown parameters. The vector $\mathbf{e}_\theta$ is used for regularization purposes. The unknown parameters are strongly uncertain, and any prior of $\boldsymbol{\theta}_0$ is non-informative.

This framework for model updating explicitly includes both measurement and modeling errors. The aim is to find the maximum a posteriori probability (MAP). The posterior PDF of λ, $\boldsymbol{\phi}$, and $\boldsymbol{\theta}$ is given as

$$p(\lambda, \boldsymbol{\phi}, \boldsymbol{\theta} | \widehat{\lambda}, \widehat{\boldsymbol{\phi}}) = K_p p(\widehat{\lambda}, \widehat{\boldsymbol{\phi}} | \lambda, \boldsymbol{\phi}, \boldsymbol{\theta}) p(\lambda, \boldsymbol{\phi} | \boldsymbol{\theta}) p(\boldsymbol{\theta}), \tag{13}$$

where the coefficient K_p results from the unknown PDF of the measured quantities $\widehat{\lambda}$ and $\widehat{\boldsymbol{\phi}}$, and it is assumed to be constant, while $p(\boldsymbol{\theta})$ is the prior PDF of $\boldsymbol{\theta}$.

In the Bayesian approach the unknown modal data λ and $\boldsymbol{\phi}$, along with the unknown parameters $\boldsymbol{\theta}$, are searched for as the most probable values. Thus, the optimization problem (P_2) is formulated as follows:

$$(\mathrm{P}_2) \qquad \begin{aligned} &\text{find} && \lambda, \ \boldsymbol{\phi}, \ \boldsymbol{\theta} \\ &\text{to minimize} && J_p(\lambda, \boldsymbol{\phi}, \boldsymbol{\theta}), \end{aligned}$$

where, using the Gaussian probability model, the objective function $J_p(\lambda, \boldsymbol{\phi}, \boldsymbol{\theta})$ is defined as the logarithm of the posterior probability (13),

$$J_p(\lambda, \boldsymbol{\phi}, \boldsymbol{\theta}) = -2 \ln p(\lambda, \boldsymbol{\phi}, \boldsymbol{\theta} | \widehat{\lambda}, \widehat{\boldsymbol{\phi}}) = \ln K_p^2 + \mathbf{e}_\mathrm{M}^{\mathrm{T}} \boldsymbol{\Sigma}_\mathrm{M}^{-1} \mathbf{e}_\mathrm{M} + \sigma_\mathcal{C}^{-2} \mathbf{e}_\mathcal{C}^{\mathrm{T}} \mathbf{e}_\mathcal{C} + \mathbf{e}_\theta^{\mathrm{T}} \boldsymbol{\Sigma}_\theta^{-1} \mathbf{e}_\theta. \tag{14}$$

In Eq. (14), $\boldsymbol{\Sigma}_\mathrm{M}$ is the diagonal covariance matrix of the measurement data that characterizes the measurement noise. The preselected coefficient $\sigma_\mathcal{C}$ represents the standard deviation of the error related to the model class $\mathcal{C}$, and $\boldsymbol{\Sigma}_\theta$ is the prior covariance matrix of

$\mathbf{e}_\theta$. The parameter σ_C expresses the relative importance of the measured modal data vs. the model class C. That is, for a large σ_C (large expected modeling error), the most probable modal data are close to the measured modal data. For a small σ_C (small expected modeling error), the most probable modal data are similar to the numerical modal data. Thus, the Bayesian framework provides a control of the trade-off between the modeling and measurement errors.

2.4. Uncertainties of identified parameters

Both methods allow for estimation of the uncertainties of the parameters θ of the updated model. The Bayesian approach allows also for estimation of the uncertainties of λ and $\boldsymbol{\phi}$. In the mode matching approach, the covariance matrix of the unknown parameters, $\widehat{\boldsymbol{\Sigma}}_\theta$, is expressed as

$$\widehat{\boldsymbol{\Sigma}}_\theta = \left(\mathbf{S}^{\mathrm{T}}(\theta)\boldsymbol{\Sigma}_{\mathrm{M}}^{-1}\mathbf{S}(\theta)\right)^{-1}, \tag{15}$$

provided the vector θ is calculated with the weighting matrix expressed as in (8). For the Bayesian approach, assuming the Gaussian probability model, the covariance matrix $\boldsymbol{\Sigma}_{\lambda\phi\theta}$ is equal to the reciprocal of the Hessian matrix $\mathbf{H}$ of the objective function $J_p(\lambda, \boldsymbol{\phi}, \theta)$,

$$\begin{aligned}\widehat{\boldsymbol{\Sigma}}_{\lambda\phi\theta} = \mathbf{H}^{-1} &= \begin{bmatrix} \frac{\partial^2 J_p}{\partial\lambda\partial\lambda^{\mathrm{T}}} & \frac{\partial^2 J_p}{\partial\lambda\partial\boldsymbol{\phi}^{\mathrm{T}}} & \frac{\partial^2 J_p}{\partial\lambda\partial\theta^{\mathrm{T}}} \\ \frac{\partial^2 J_p}{\partial\boldsymbol{\phi}\partial\lambda^{\mathrm{T}}} & \frac{\partial^2 J_p}{\partial\boldsymbol{\phi}\partial\boldsymbol{\phi}^{\mathrm{T}}} & \frac{\partial^2 J_p}{\partial\boldsymbol{\phi}\partial\theta^{\mathrm{T}}} \\ \frac{\partial^2 J_p}{\partial\theta\partial\lambda^{\mathrm{T}}} & \frac{\partial^2 J_p}{\partial\theta\partial\boldsymbol{\phi}^{\mathrm{T}}} & \frac{\partial^2 J_p}{\partial\theta\partial\theta^{\mathrm{T}}} \end{bmatrix}^{-1} = \\ &= \begin{bmatrix} \sigma_C^{-2}\mathbf{G}_\lambda + [\boldsymbol{\Sigma}_{\mathrm{M}}^{-1}]_{\lambda\lambda} & -2\sigma_C^{-2}\mathbf{L}_1 + [\boldsymbol{\Sigma}_{\mathrm{M}}^{-1}]_{\lambda\phi}\mathbf{L}_0 & -\sigma_C^{-2}\mathbf{L}_2 \\ & \sigma_C^{-2}\mathbf{G}_\phi + \mathbf{L}_0^{\mathrm{T}}[\boldsymbol{\Sigma}_{\mathrm{M}}^{-1}]_{\phi\phi}\mathbf{L}_0 & \sigma_C^{-2}\mathbf{L}_3 \\ \textit{symmetric} & & \sigma_C^{-2}\mathbf{G}_\theta^{\mathrm{T}}\mathbf{G}_\theta + \boldsymbol{\Sigma}_\theta^{-1} \end{bmatrix}^{-1}, \end{aligned} \tag{16}$$

where:

$$\mathbf{L}_1 = \begin{bmatrix} \boldsymbol{\phi}^{(1)\mathrm{T}}\mathbf{M}(\mathbf{K}(\theta) - \lambda_1\mathbf{M}) & & \mathbf{0} \\ & \ddots & \\ \mathbf{0} & & \boldsymbol{\phi}^{(N_m)\mathrm{T}}\mathbf{M}(\mathbf{K}(\theta) - \lambda_{N_m}\mathbf{M}) \end{bmatrix}, \quad \mathbf{L}_2^{(t\text{th col.})} = \begin{bmatrix} \boldsymbol{\phi}^{(1)\mathrm{T}}\mathbf{M}\mathbf{K}_t\boldsymbol{\phi}^{(1)} \\ \vdots \\ \boldsymbol{\phi}^{(N_m)\mathrm{T}}\mathbf{M}\mathbf{K}_t\boldsymbol{\phi}^{(N_m)} \end{bmatrix},$$

$$\mathbf{L}_3^{(t\text{th col.})} = \begin{bmatrix} \left[(\mathbf{K}(\theta) - \lambda_1\mathbf{M})\mathbf{K}_t + \mathbf{K}_t(\mathbf{K}(\theta) - \lambda_1\mathbf{M})\right]\boldsymbol{\phi}^{(1)} \\ \vdots \\ \left[(\mathbf{K}(\theta) - \lambda_{N_m}\mathbf{M})\mathbf{K}_t + \mathbf{K}_t(\mathbf{K}(\theta) - \lambda_{N_m}\mathbf{M})\right]\boldsymbol{\phi}^{(N_m)} \end{bmatrix}, \quad \mathbf{G}_\lambda = \begin{bmatrix} \boldsymbol{\phi}^{(1)\mathrm{T}}\mathbf{M}^2\boldsymbol{\phi}^{(1)} & & \mathbf{0} \\ & \ddots & \\ \mathbf{0} & & \boldsymbol{\phi}^{(N_m)\mathrm{T}}\mathbf{M}^2\boldsymbol{\phi}^{(N_m)} \end{bmatrix},$$

$$\mathbf{G}_\phi = \begin{bmatrix} (\lambda_1\mathbf{M} - \mathbf{K}(\theta))^2 & & \mathbf{0} \\ & \ddots & \\ \mathbf{0} & & (\lambda_{N_m}\mathbf{M} - \mathbf{K}(\theta))^2 \end{bmatrix}, \quad \mathbf{G}_\theta = \begin{bmatrix} \mathbf{K}_1\boldsymbol{\phi}^{(1)} & \cdots & \mathbf{K}_{N_\theta}\boldsymbol{\phi}^{(1)} \\ \vdots & \vdots & \vdots \\ \mathbf{K}_1\boldsymbol{\phi}^{(N_m)} & \cdots & \mathbf{K}_{N_\theta}\boldsymbol{\phi}^{(N_m)} \end{bmatrix},$$

and the subscripts of the reciprocal covariance matrix $\boldsymbol{\Sigma}_{\mathrm{M}}^{-1}$ indicate the block that corresponds to the respective variables: eigenvalues ($\lambda\lambda$) or mode shapes ($\phi\phi$).

In both cases the covariance matrices are not diagonal. The variances of the identified parameters are located on the diagonal of the covariance matrices.

2.5. Bias–variance trade-off

The estimation error consists of the systematic error (bias) and the covariance error. The more measurement data is available in relation to the number of unknown parameters, the smaller the parameter variances are. Conversely, utilization of a more sophisticated model (with a larger number of unknown parameters) with the same set of measurement data decreases the bias error at the expense of higher parameter variances. This interplay between the bias and the variance is known as the bias–variance trade-off. It can be affected using the technique called regularization, which provides means to balance the relative importance of the measurement data and the numerical model. In case of the Bayesian approach described in Section 2.3, regularization intensity is controlled by the parameter σ_C.

Mode matching can also be formulated and classified as a MAP problem. It results in an additional regularization term added to the objective function defined in Eq. (5). Assuming the Gaussian probability model and using Eq. (8), the objective function becomes:

$$\varepsilon_p(\theta) = -2\ln p(\theta|\widehat{\lambda}, \widehat{\boldsymbol{\phi}}) = -2\ln K_p p(\widehat{\lambda}, \widehat{\boldsymbol{\phi}}|\theta)p(\theta) = \ln K_p^2 + \mathbf{e}^{\mathrm{T}}(\theta)\boldsymbol{\Sigma}_{\mathrm{M}}^{-1}\mathbf{e}(\theta) + \mathbf{e}_\theta^{\mathrm{T}}\boldsymbol{\Sigma}_\theta^{-1}\mathbf{e}_\theta. \tag{17}$$

The additional regularization term is related to the prior probability density function $p(\theta)$. Without it, minimization of the objective function corresponds to finding the maximum likelihood estimator.

Ostrowski et al. [15] applied regularization as in Eq. (17) and investigated the influence of measurement noise on parametric identification when only few first vibration modes were measured due to equipment limitations. However, this paper considers

examples with sufficient amount of measurement data (in comparison to the number of unknown parameters), so that additional regularization with the term $\mathbf{e}_\theta^{\mathrm{T}} \boldsymbol{\Sigma}_\theta^{-1} \mathbf{e}_\theta$ is not necessary. Mode matching without regularization (that is, searching for the maximum likelihood) is thus used in the following, as described in Section 2.2.

In the MAP formulation described in Section 2.3, the prior term $\mathbf{e}_\theta^{\mathrm{T}} \boldsymbol{\Sigma}_\theta^{-1} \mathbf{e}_\theta$ is also less important due to abundant measurement data. A covariance matrix $\boldsymbol{\Sigma}_\theta$ with large entries is thus used, which corresponds to a limited knowledge or a lack of a prior knowledge about $\boldsymbol{\theta}$. However, an intense regularization by means of σ_C is still necessary due to the use of an objective function that allows to avoid the mode matching problem. Measured data cannot be directly used in Eq. (11), as the measured mode shapes have to be expanded to the DOFs of the FE model and due to the sensitivity of this norm to the measurement noise [3]. Regularization is provided by replacing in Eq. (11) the measurement data with the introduced random variables λ_m and $\boldsymbol{\phi}^{(m)}$.

2.6. Minimization algorithms

This subsection discusses the optimization methods used to minimize the objective functions in both considered methods.

2.6.1. Mode matching: Gauss–Newton minimization

The objective function is a quadratic form with respect to $\mathbf{e}$. However, solving the optimization problem (P_1) is not straightforward due to the nonlinear dependence of the numerical modal data $\lambda_m^{\mathrm{num}}(\boldsymbol{\theta})$ and $\boldsymbol{\phi}_{\mathrm{num}}^{(m)}(\boldsymbol{\theta})$ on the unknown parameters $\boldsymbol{\theta}$. A widely accepted method for minimization of such objective functions is the Gauss–Newton method [33]. Friswell and Mottershead [1] adopted this method for various problems of model updating. It is employed in this paper, and in each iteration step the modal data are locally linearized with respect to the increment $\Delta\boldsymbol{\theta}$. This yields the following function to be minimized in each step of the optimization procedure:

$$J_\varepsilon(\Delta\boldsymbol{\theta}) = \left(\mathbf{S}(\boldsymbol{\theta})\Delta\boldsymbol{\theta} - \mathbf{e}(\boldsymbol{\theta})\right)^{\mathrm{T}} \mathbf{W} \left(\mathbf{S}(\boldsymbol{\theta})\Delta\boldsymbol{\theta} - \mathbf{e}(\boldsymbol{\theta})\right), \tag{18}$$

where $\mathbf{S}(\boldsymbol{\theta})$ is the Jacobian matrix of the numerical modal parameters with respect to $\boldsymbol{\theta}$. By pursuing $\nabla J_\varepsilon(\Delta\boldsymbol{\theta}) = \mathbf{0}$, the following equation is obtained:

$$\mathbf{S}^{\mathrm{T}}(\boldsymbol{\theta})\mathbf{W}\mathbf{S}(\boldsymbol{\theta})\Delta\boldsymbol{\theta} = \mathbf{S}^{\mathrm{T}}(\boldsymbol{\theta})\mathbf{W}\mathbf{e}(\boldsymbol{\theta}). \tag{19}$$

Finally, the values of the unknown parameters are updated in each iteration step as follows:

$$\boldsymbol{\theta}_{k+1} = \boldsymbol{\theta}_k + \kappa_\theta \Delta\boldsymbol{\theta}_k = \boldsymbol{\theta}_k + \kappa_\theta \left(\mathbf{S}^{\mathrm{T}}(\boldsymbol{\theta}_k)\mathbf{W}\mathbf{S}(\boldsymbol{\theta}_k)\right)^{-1} \mathbf{S}^{\mathrm{T}}(\boldsymbol{\theta}_k)\mathbf{W}\mathbf{e}(\boldsymbol{\theta}_k), \tag{20}$$

where k indexes the iteration steps, and the scaling factor κ_θ is determined by trial and error. The objective function in Eq. (17) can also be minimized with the Gauss–Newton method analogously, as demonstrated in works [13–15].

2.6.2. Bayesian approach: alternating subspace search

An iterative minimization procedure has been adopted here, as proposed by Yuen et al. [3,23]. Each iteration step is divided into three substeps, at which the objective function J_p is consecutively minimized with respect to only one of λ, $\boldsymbol{\phi}$, or $\boldsymbol{\theta}$, while the other two are treated as constant. Such an approach allows J_p to be handled at each substep as a quadratic function. In the initialization step $\boldsymbol{\theta}_{k=1} = \boldsymbol{\theta}_0$ and $\lambda_{k=1} = \widehat{\lambda}$ are selected, and $\mathbf{K}(\boldsymbol{\theta}_{k=1})$ is calculated. Then, in the kth iteration step, the following substeps are implemented:

$$\begin{aligned}
\boldsymbol{\phi}_{k+1} &= \arg\min_{\boldsymbol{\phi}} J_p(\lambda_k, \boldsymbol{\phi}, \boldsymbol{\theta}_k) = \\
&= \left(\sigma_C^{-2}\mathbf{G}_\phi + \mathbf{L}_0^{\mathrm{T}}[\boldsymbol{\Sigma}_{\mathrm{M}}^{-1}]_{\phi\phi}\mathbf{L}_0\right)^{-1} \mathbf{L}_0^{\mathrm{T}} \left([\boldsymbol{\Sigma}_{\mathrm{M}}^{-1}]_{\phi\lambda}(\widehat{\lambda} - \lambda_k) + [\boldsymbol{\Sigma}_{\mathrm{M}}^{-1}]_{\phi\phi}\widehat{\boldsymbol{\psi}}\right),
\end{aligned} \tag{21}$$

$$\begin{aligned}
\lambda_{k+1} &= \arg\min_{\lambda} J_p(\lambda, \boldsymbol{\phi}_{k+1}, \boldsymbol{\theta}_k) = \\
&= \left(\sigma_C^{-2}\mathbf{G}_\lambda + [\boldsymbol{\Sigma}_{\mathrm{M}}^{-1}]_{\lambda\lambda}\right)^{-1} \left(\sigma_C^{-1}\mathbf{g}_\lambda + [\boldsymbol{\Sigma}_{\mathrm{M}}^{-1}]_{\lambda\lambda}\widehat{\lambda}_k + [\boldsymbol{\Sigma}_{\mathrm{M}}^{-1}]_{\lambda\phi}(\widehat{\boldsymbol{\psi}} - \mathbf{L}_0\boldsymbol{\phi}_{k+1})\right),
\end{aligned} \tag{22}$$

$$\begin{aligned}
\boldsymbol{\theta}_{k+1} &= \arg\min_{\boldsymbol{\theta}} J_p(\lambda_{k+1}, \boldsymbol{\phi}_{k+1}, \boldsymbol{\theta}) = \\
&= \left(\sigma_C^{-2}\mathbf{G}_\theta^{\mathrm{T}}\mathbf{G}_\theta + \boldsymbol{\Sigma}_\theta^{-1}\right)^{-1} \left(\mathbf{G}_\theta^{\mathrm{T}}\mathbf{g}_\theta + \boldsymbol{\Sigma}_\theta^{-1}\boldsymbol{\theta}_0\right),
\end{aligned} \tag{23}$$

where:

$$\mathbf{g}_\lambda = \begin{bmatrix} \boldsymbol{\phi}_{k+1}^{(1)\mathrm{T}}\mathbf{M}\mathbf{K}(\boldsymbol{\theta}_k)\boldsymbol{\phi}_{k+1}^{(1)} \\ \vdots \\ \boldsymbol{\phi}_{k+1}^{(N_m)\mathrm{T}}\mathbf{M}\mathbf{K}(\boldsymbol{\theta}_k)\boldsymbol{\phi}_{k+1}^{(N_m)} \end{bmatrix}, \qquad \mathbf{g}_\theta = \begin{bmatrix} (\lambda_1\mathbf{M} - \mathbf{K}_0)\boldsymbol{\phi}_{k+1}^{(1)} \\ \vdots \\ (\lambda_{N_m}\mathbf{M} - \mathbf{K}_0)\boldsymbol{\phi}_{k+1}^{(N_m)} \end{bmatrix}.$$

The above minimization approach has the advantage that it does not require calculation nor inversion of full Hessian matrix (Eq. (16)). However, it may result in a slow convergence in certain cases, as shown further in this paper. It is due to the alternating minimization in the three subspaces, which has similar properties to the steepest/coordinate descent. The Gauss–Newton or, more generally, Newton optimization approaches cannot be used due to severe ill-conditioning of the Hessian matrix, as evidenced in case of structures considered in this paper.

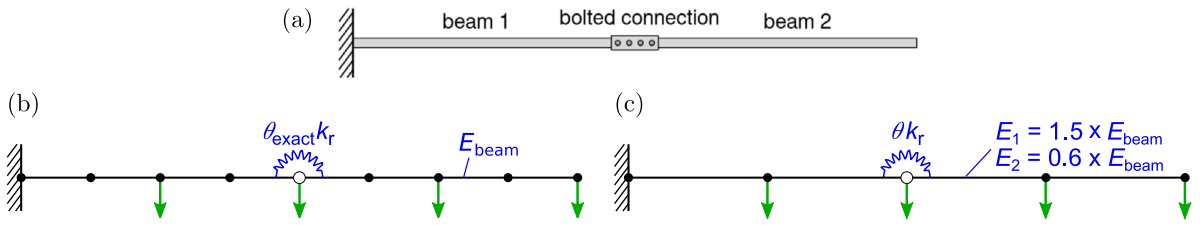

Fig. 3. (a) Scheme of a structure with a bolted connection; (b) the FE model representing the measured system; (c) the FE model to be updated including the modeling errors. The green arrows denote measured DOFs.

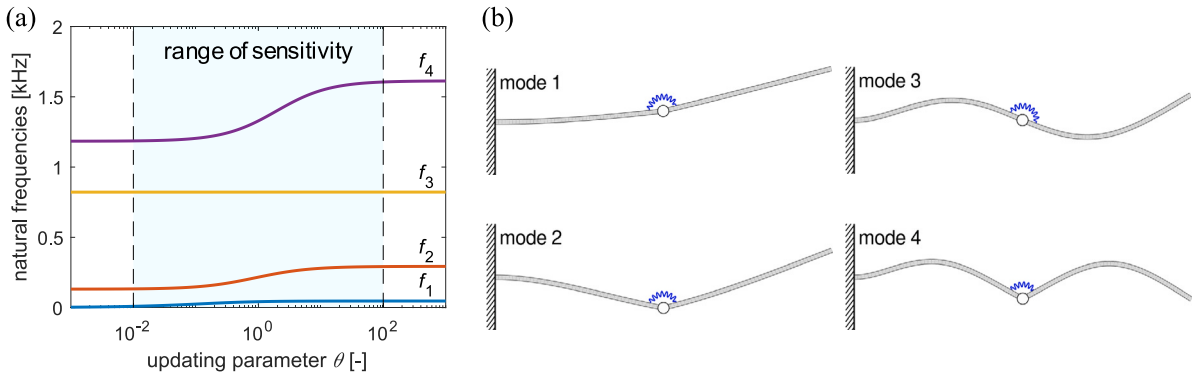

Fig. 4. (a) Dependence of the first four natural frequencies of the beam structure on the parameter θ, and (b) the corresponding mode shapes for $\theta = 0.5$.

2.7. Illustrative example

This subsection illustrates the challenges in vibration-based identification of stiffness parameters. A cantilever beam with a bolted connection at its midpoint is considered, as depicted in Fig. 3. It has a length of $L = 0.6$ m and is made of steel with $E_{beam} = 2.1 \cdot 10^{11}$ Pa and $\rho = 7840$ kg/m^3. Its cross-section is the same as in the view "A–A" in Fig. 8. The bolted connection is assumed to be weightless and represented by the rotational stiffness $k_r = E_{beam} I / L = 3887.6$ Nm/rad between the involved rotational DOFs, where $I = 5.55 \cdot 10^{-9}$ m^4 is the second moment of area of the cross-section. This stiffness is scaled by the parameter θ.

The dependence of the first four natural frequencies on the stiffness of the bolted connection, expressed in terms of the scaling parameter θ, is plotted in Fig. 4a. A sensitivity range can be observed in which most frequencies depend on θ. Below this range, the bolted connection behaves like a hinge, and above this range, it acts as a semi-rigid node. Identifying the stiffness parameter outside this sensitivity range can be challenging or even impossible. The third natural frequency is insensitive to the parameter θ. Fig. 4b illustrates the first four mode shapes for $\theta = 0.5$, and the third mode shape indeed does not involve bending of the connection.

For the Bayesian approach, proper selection of weighting parameters is not straightforward. Their influence on the error of the identified parameters is discussed. The FE model depicted in Fig. 3b is treated as the measured physical system. The rotational stiffness parameter of the bolted connection, which is to be identified, has a value of $\theta_{exact} = 0.5$. The FE model to be updated is similar, but it has a two times sparser FE mesh (Fig. 3c). The Young's modulus of the beams in this model:

- in CASE I: $E_1 = 1.5 E_{beam}$, meaning the Young's modulus is overestimated;
- in CASE II: $E_2 = 0.6 E_{beam}$, meaning the Young's modulus is underestimated.

These differences in mesh and material properties represent modeling errors. The measured DOFs are denoted by green arrows in Fig. 3a and b.

The covariance matrix $\boldsymbol{\Sigma}_M$ is diagonal and corresponds to a coefficient of variation (CoV) of the modal data equal to 1%. Gaussian noise with a respective level was added to the modal data extracted from the FE model representing the measured system. A one-element covariance matrix $\boldsymbol{\Sigma}_\theta = [100]$ was used to reflect the high assumed uncertainty of θ. The results of the Bayesian approach are compared to those of the mode matching method. The error metric ε is calculated using the weighting matrix $\mathbf{W}$ specified in Eq. (8). In the Bayesian approach, it quantifies the fit of the model to the measurement data and is not used during optimization.

Stopping conditions are different for CASE I and CASE II due to very different convergence patterns. The maximum number of iteration steps is limited to 200 in CASE I and $2 \cdot 10^5$ in CASE II. In all cases, the search is also stopped in the kth iteration, if the update $\Delta\theta_k$ satisfies $|\Delta\theta_k|/\theta_k < 2^{-52}$ (floating point relative accuracy).

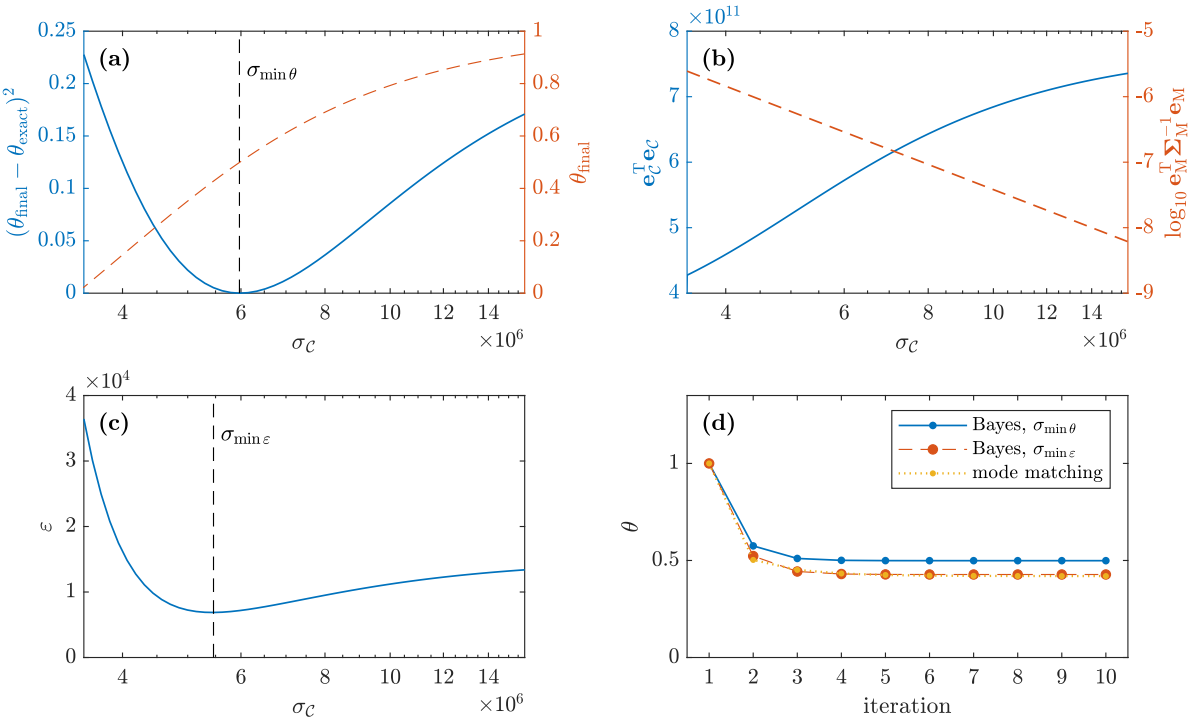

Fig. 5. Influence of the parameter $\sigma_{\mathcal{C}}$ on the updating procedure for the model with an overestimated Young modulus (CASE I): (a) error and final value of updated parameter θ, (b) modeling and measurement error, (c) error between numerical and measured modal data ε, and (d) first 10 iteration steps of evolution of the unknown parameter θ during the updating procedure for $\sigma_{\mathcal{C}} = \sigma_{\min\theta}$ and $\sigma_{\mathcal{C}} = \sigma_{\min\varepsilon}$ compared with mode matching.

CASE I. The Bayesian model updating procedure was performed for different values of the weighting parameter $\sigma_{\mathcal{C}}$. The dependence of the final updated value of the joint stiffness θ on $\sigma_{\mathcal{C}}$, along with its error, the modeling error ($\mathbf{e}_{\mathcal{C}}^{\mathrm{T}}\mathbf{e}_{\mathcal{C}}$), the measurement error ($\mathbf{e}_{\mathrm{M}}^{\mathrm{T}}\boldsymbol{\Sigma}_{\mathrm{M}}^{-1}\mathbf{e}_{\mathrm{M}}$), and the error ε between experimental and numerical modal data (Eq. (5)) is presented in Fig. 5. The minimum error of the identified θ does not correspond to the minimum value of ε due to modeling errors, which are the overestimated Young modulus and crude discretization. The modeling error metric $\mathbf{e}_{\mathcal{C}}^{\mathrm{T}}\mathbf{e}_{\mathcal{C}}$ also does not correspond with ε. As noted in Section 2.3, a lower value of $\mathbf{e}_{\mathcal{C}}^{\mathrm{T}}\mathbf{e}_{\mathcal{C}}$ does not necessarily indicate a better fit of the model to the measurement data. This is because a lower $\sigma_{\mathcal{C}}$ results in the most probable modal parameters ($\boldsymbol{\lambda}$ and $\boldsymbol{\phi}$) being closer to the numerical values obtained from the FE model, thereby reducing the modeling error $\mathbf{e}_{\mathcal{C}}$ as per the eigenvalue formulation Eq. (11). Conversely, an overestimated value of $\sigma_{\mathcal{C}}$ can result in a higher modeling error $\mathbf{e}_{\mathcal{C}}^{\mathrm{T}}\mathbf{e}_{\mathcal{C}}$ as the most probable modal data are then close to the measured data, resulting in a smaller measurement error $\mathbf{e}_{\mathrm{M}}^{\mathrm{T}}\boldsymbol{\Sigma}_{\mathrm{M}}^{-1}\mathbf{e}_{\mathrm{M}}$ at the cost of a higher modeling error.

For $\sigma_{\mathcal{C}} < \sigma_{\min\theta}$ stiffness of the bolted connection is underestimated (Fig. 5a), while for $\sigma_{\mathcal{C}} > \sigma_{\min\theta}$ it is overestimated. The dependence of the estimate on $\sigma_{\mathcal{C}}$ is monotonic and almost linear. For $\sigma_{\mathcal{C}}$ smaller than the lower limit of the considered range, θ is estimated as zero or even negative, which results in numerical instabilities.

Fig. 5d depicts the evolution of the unknown parameter θ obtained for two different values of $\sigma_{\mathcal{C}}$, as well as using the mode matching method. The parameter that was identified for $\sigma_{\mathcal{C}} = \sigma_{\min\varepsilon}$, which provides the minimum error ε, was approximately 20% smaller than the exact value and is similar to the result obtained using the mode matching method. A minimum value of ε was achieved by compensating for the overestimation of Young's modulus, as seen in Figs. 3c and 5d. In practice, selecting $\sigma_{\mathcal{C}}$ close to $\sigma_{\mathcal{C}} = \sigma_{\min\theta}$ is not straightforward. In this example, it was accomplished through full enumeration and assuming that the exact value of the rotational stiffness is known. Such information is not available in real systems.

For all $\sigma_{\mathcal{C}}$ within the range shown in Figs. 5a-c, both the most probable mode shapes and the numerical mode shapes are well-correlated with these obtained from the FE model that represents the measured system (Fig. 4b). Thus, they are not separately plotted.

Parameter uncertainties have been calculated for both the mode matching method and the Bayesian approach. In the former case, the CoV of the estimated unknown parameter was $V^{\theta} = 4.44 \cdot 10^{-5}$ (Eq. (15)). In the later case, the estimation of uncertainty is not straightforward due to the ill-conditioning of the Hessian matrix $\mathbf{H}$ (Eq. (16)). The covariance matrix $\widehat{\boldsymbol{\Sigma}}_{\lambda\phi\theta}$ cannot be calculated as a direct inverse of $\mathbf{H}$ because the condition number of $\mathbf{H}$ is as high as $1.2 \cdot 10^{16}$. Hence, it was computed using regularization via truncated singular value decomposition (TSVD). The matrix $\mathbf{H}$ was first decomposed into $\mathbf{H} = \mathbf{U}\mathbf{S}\mathbf{V}^{\mathrm{T}}$, where $\mathbf{S} = \mathrm{diag}(s_1, s_2, \ldots s_{N_s})$ is a diagonal matrix containing singular values of $\mathbf{H}$, while $\mathbf{U}$ and $\mathbf{V}$ are unitary matrices that collect the left and right singular vectors of $\mathbf{H}$. The regularized inverse of $\mathbf{H}$ is then given as

$$\widetilde{\boldsymbol{\Sigma}}_{\lambda\phi\theta}(s_{\mathrm{tol}}) = \widetilde{\mathbf{V}}(s_{\mathrm{tol}})\widetilde{\mathbf{S}}^{-1}(s_{\mathrm{tol}})\widetilde{\mathbf{U}}^{\mathrm{T}}(s_{\mathrm{tol}}), \tag{24}$$

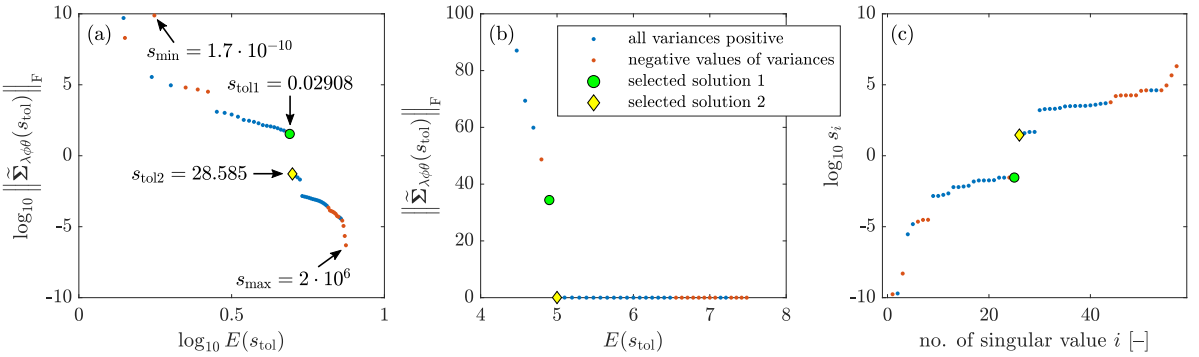

Fig. 6. Regularization of the covariance matrix $\widetilde{\boldsymbol{\Sigma}}_{\lambda\phi\theta}(s_{\text{tol}})$ in CASE I: (a) L-curve; (b) L-curve in the region around the selected s_{tol1} and s_{tol2}, shown in a lin–lin scale; (c) singular value spectrum of $\mathbf{H}$. Solutions 1 and 2 correspond to two adjacent values of the variances of the identified θ that are significantly higher and significantly lower, respectively, than the one calculated by mode matching.

where $\widetilde{\mathbf{S}}(s_{\text{tol}})$ is a matrix obtained from $\mathbf{S}$ by removing its columns and rows corresponding to the singular values s_i that are less than a tolerance value s_{tol}, and the matrices $\widetilde{\mathbf{U}}(s_{\text{tol}})$ and $\widetilde{\mathbf{V}}(s_{\text{tol}})$ contain the corresponding remaining left and right singular vectors.

The appropriate value of s_{tol} is selected using the L-curve method, which analyzes the dependence of the Frobenius norm $\left\| \widetilde{\boldsymbol{\Sigma}}_{\lambda\phi\theta}(s_{\text{tol}}) \right\|_{\text{F}}$ on the error metric

$$E(s_{\text{tol}}) = \left\| \frac{1}{2} \left(\mathbf{H} \widetilde{\boldsymbol{\Sigma}}_{\lambda\phi\theta}(s_{\text{tol}}) + \widetilde{\boldsymbol{\Sigma}}_{\lambda\phi\theta}(s_{\text{tol}}) \mathbf{H} \right) - \mathbf{I} \right\|_{\text{F}}, \tag{25}$$

as obtained for various levels of the truncation threshold s_{tol}. Fig. 6a displays the entire L-curve, while Fig. 6b focuses on the region around the selected threshold. Due to ill-conditioning, the computed values of $\mathbf{H}\widetilde{\boldsymbol{\Sigma}}_{\lambda\phi\theta}(s_{\text{tol}})$ and $\widetilde{\boldsymbol{\Sigma}}_{\lambda\phi\theta}(s_{\text{tol}})\mathbf{H}$ might not be equal, hence their mean is used in Eq. (25). The solutions for which some of the computed variances on the diagonal of $\widetilde{\boldsymbol{\Sigma}}_{\lambda\phi\theta}(s_{\text{tol}})$ are negative are indicated with red dots. The corresponding singular value spectrum is presented in Fig. 6c.

The characteristic corner, which is typical of L-curves, is not distinguishable in Fig. 6a plotted in log–log scale, making it difficult to select an appropriate value of σ_{tol}. Two adjacent solutions were thus selected based on the corner visible in lin–lin scale (Fig. 6b). The first solution, represented by a green dot, has a CoV of $V^{\theta} = 2.3 \cdot 10^{-2}$, which is significantly higher than that calculated through mode matching. The CoV for the second solution, represented by a yellow diamond, is $V^{\theta} = 1.45 \cdot 10^{-7}$, which is significantly lower. This indicates that the calculated uncertainty in the Bayesian approach is highly dependent on the selected threshold s_{tol} and may be influenced by ill-conditioning. The larger the s_{tol}, the smaller the norm $\left\| \widetilde{\boldsymbol{\Sigma}}_{\lambda\phi\theta}(s_{\text{tol}}) \right\|_{\text{F}}$ and the variances become. As a result, the reliability of the estimated uncertainties cannot be guaranteed. This example does not discuss the variances of the most probable modal parameters $\boldsymbol{\lambda}$ and $\boldsymbol{\phi}$, but these are investigated in the experimental example presented in Section 4.4.

CASE II. The results obtained for the underestimated Young's modulus are shown in Fig. 7. Unlike in CASE I, the value of θ found using the Bayesian approach is overestimated for each σ_C (Fig. 7). In this case, $\sigma_{\min\theta} = \sigma_{\min\varepsilon}$, and the trade-off between measurement and numerical errors is less pronounced. Similar as the mode matching, the Bayesian method also tends to fit model to the measurement data when the optimal σ_C is selected. However, as shown in Fig. 7d, the mode matching method estimates the unknown parameter θ closer to its exact value θ_{exact}. Moreover, mode matching yields a significantly lower value of $\varepsilon = 2.93 \cdot 10^{5}$, which is about two times smaller than that obtained using the Bayesian approach with the optimal σ_C (Fig. 7c).

The mode matching method finds the estimate of the unknown parameter in a few iterations, whereas the parameter estimated using the Bayesian approach slowly converges to its final value over more than $2 \cdot 10^4$ iterations. This contrasts with CASE I, where no more than 10 iterations were needed. The minimization process utilizing the alternating subspace search, described in Section 2.6.2, may encounter convergence problems when dealing with a complex objective function (e.g., with a trough-like shape). Here, the objective function is influenced by the change of the Young modulus. It has been observed that the rate of convergence is highly dependent on factors such as the Young modulus, initial parameter θ_0, and the measured vibration modes. This stands in contrast to mode matching, which employs the Gauss–Newton minimization algorithm and proves to be generally robust in regard to these factors. Convergence problems are also encountered in the experimental and large-scale examples described later in this paper, and they can be challenging to remedy.

The Bayesian approach yields for $\sigma_C = \sigma_{\min\theta}$ acceptable results, as evidenced in Fig. 7d. However, the obtained third most probable mode shape is not well-correlated with its measured counterpart (compare Fig. 7e and 4b). The MAC (Eq. (26)) between these mode shapes for $\sigma_C = 10^{1.8}$ is equal to 0.314, whereas for the third numerical mode shape it is 0.999. For $\sigma_C > \sigma_{\min\theta}$, all the most probable mode shapes are well-correlated with the corresponding measured shapes, e.g., for $\sigma_C = 10^{2.4}$ the MAC between the third most probable mode shape and the measured shape is 0.999. This change in correlation of the third most probable mode shape results in a sudden change of various error metrics at $\sigma_C = \sigma_{\min\theta}$, as seen in Fig. 7a-c. The parameter θ turns out to be strongly overestimated when all the most probable mode shapes are well-correlated with the measured shapes, and it is closer to its exact value (even if still overestimated) only when one of the most probable modes shapes is not well-correlated with the measured shape. It shows the sensitivity of the Bayesian method to the selected value of σ_C. In contrast, the mode matching method performs robustly also with the underestimated Young modulus and yields almost exact results.

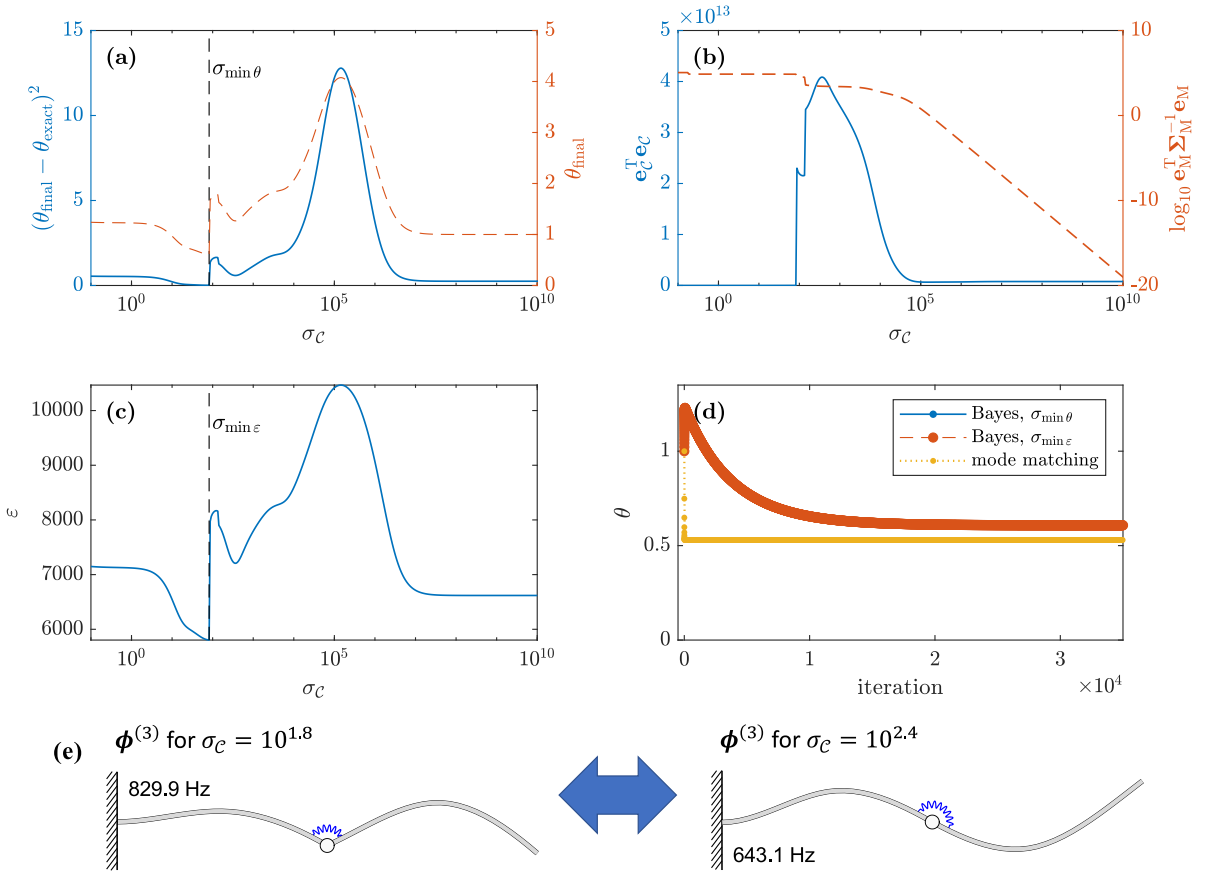

Fig. 7. The influence of the σ_C parameter on updating procedure of the model with underestimated Young modulus (CASE II): (a) error and final value of updated parameter θ, (b) modeling and measurement error, (c) error between numerical and measured modal data ε, (d) evolution of unknown parameter θ during updating procedure for $\sigma_C = \sigma_{\min\theta}$ and $\sigma_C = \sigma_{\min\varepsilon}$ compared with mode matching, and (e) the third most probable mode shape identified for σ_C parameter slightly lower and slightly larger than $\sigma_C = \sigma_{\min\theta}$.

3. Structure under investigation

The frame structure used in experimental tests is shown in Figs. 8a (schematic) and 8b (photograph). It has six semi-actively lockable joins, which were in the locked state during the experiments, and thus, they are treated as rigid bodies. They connect to structural beams via bolted connections, whose stiffness parameters are highly uncertain and require identification. Further information on the joints can be found in [34–36]. Fig. 9a shows a joint with details of the bolted connection. The structure is fixed to the support as depicted in Fig. 8b.

3.1. Finite element model

The lab structure is modeled using a 2D FE model (Fig. 10a). The bolted connections are represented by their rotational stiffness, parameterized as described in Section 2.1. The joints are modeled as rigid bodies with mass $m_{\mathrm{J}} = 1.86$ kg and mass moment of inertia $I_{\mathrm{J}} = 1.55 \cdot 10^{-3}$ kg/m^2 and represented as offsets between the respective nodes in the FE mesh, similar to the coupler shown in Fig. 2b. The nominal rotational stiffness of each bolted connection is $k_{\mathrm{R}} = 10^4$ Nm/rad. The nominal stiffness of the beam profiles corresponds to the Young's modulus of steel $E = 2.1 \cdot 10^5$ MPa, while their material density is $\rho = 7840$ kg/m^3. The FE model employs finite elements with 6 DOFs and cubic shape functions based on the Euler–Bernoulli beam theory. The total number of DOFs in the FE model is $N_{\mathrm{d}} = 139$.

The sensitivity of modal parameters to the rotational stiffness of the bolted connections is analyzed as discussed in Section 2.7. Fig. 9b shows the dependence of the first 10 natural frequencies obtained from the FE model on the rotational stiffness of the bolted connections. A common scaling parameter θ is used for all 16 bolted connections, that is, $\boldsymbol{\theta} = \mathbf{1}\theta$, where $\mathbf{1}$ is a vector of ones with the appropriate dimension. The natural frequencies are represented by dotted lines, while the solid lines indicate the frequencies of

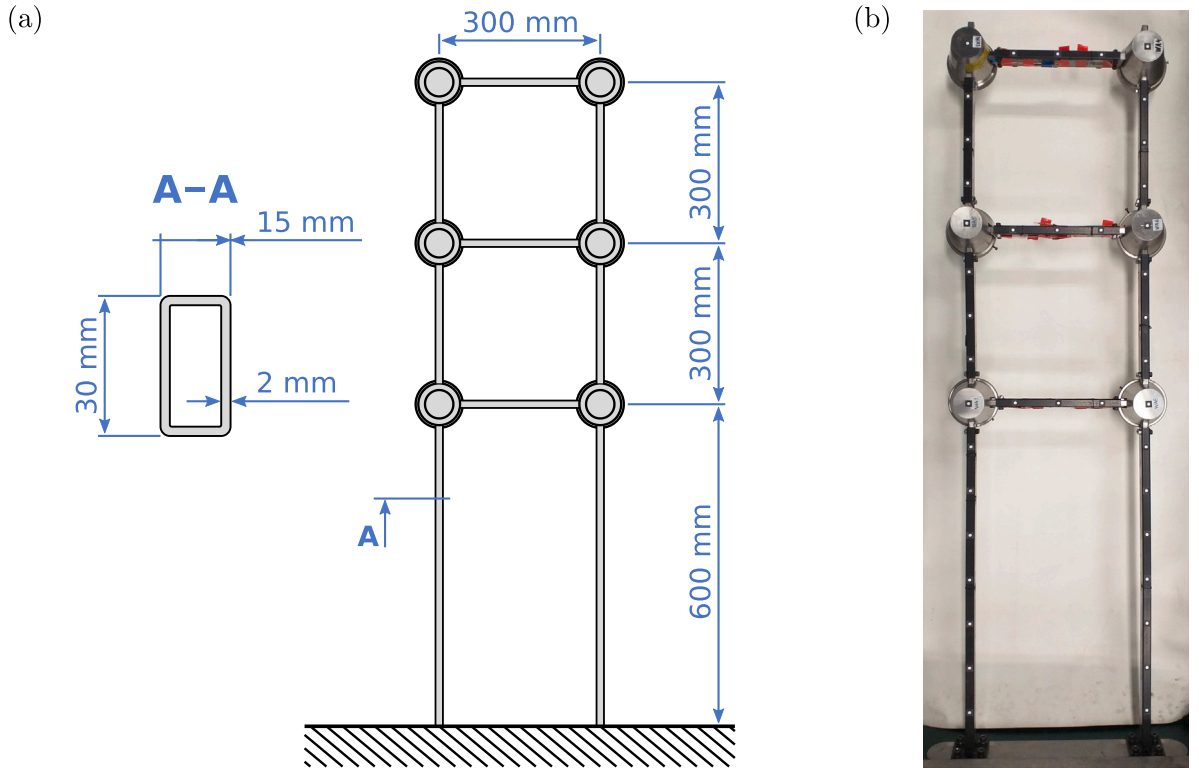

Fig. 8. Considered frame structure: (a) scheme and dimensions, (b) photo of the laboratory rig.

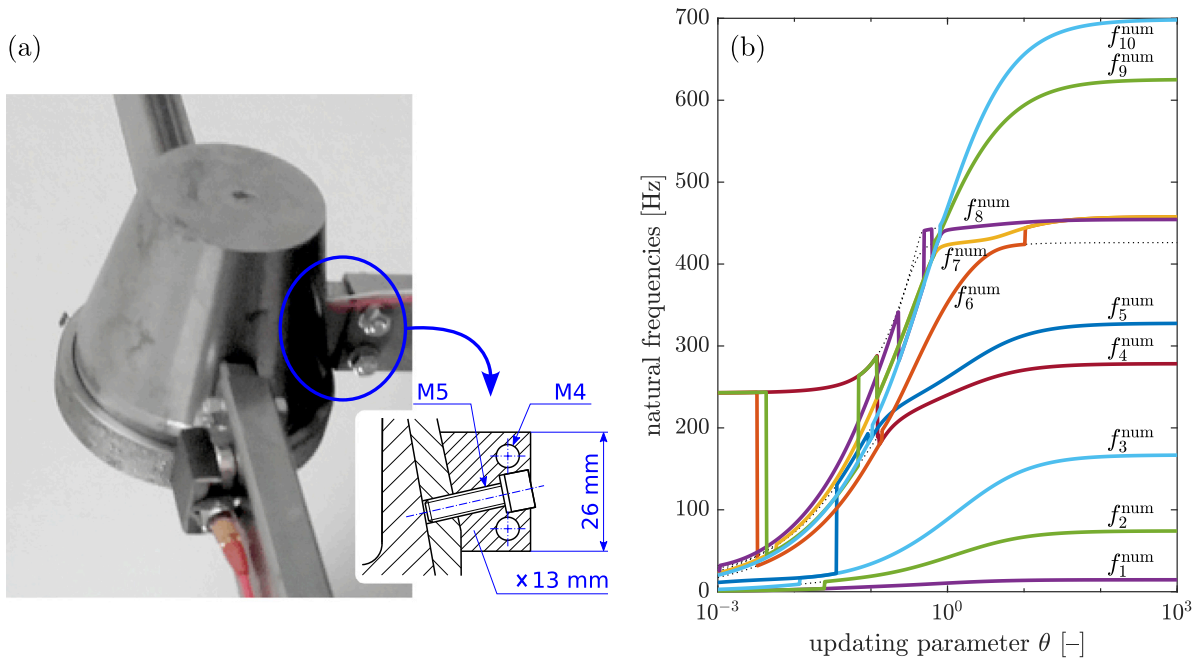

Fig. 9. (a) Joint with bolted connections, (b) dependence of natural frequencies (dotted lines) and natural frequencies matched with those obtained for $\theta = 1$ (solid lines) on the rotational stiffness of the bolted connections. The nominal rotational stiffness of each bolted connection is $k_R = 10^4$ Nm/rad.

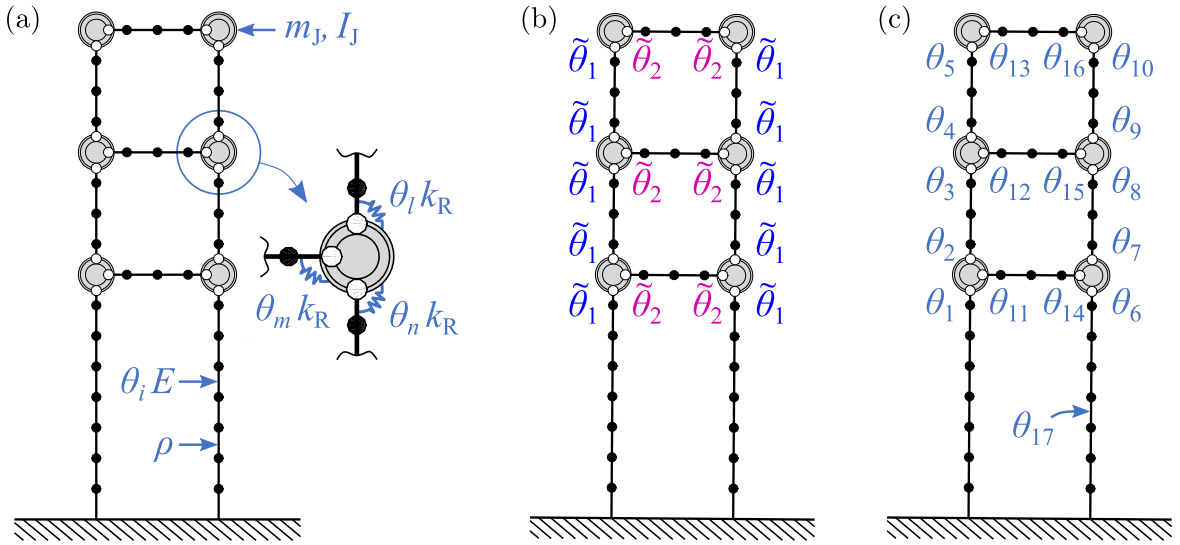

Fig. 10. FE model of the considered structure: (a) FE mesh and parameterization of bolted connections and beam Young's modulus, (b) simplified parameterization for initial model updating, (c) numbering of parameters for precise model updating.

the modes that best match the successive modes obtained for $\theta = 1$, based on the modal assurance criterion (MAC):

$$\mathrm{MAC}\left(\boldsymbol{\phi}^{(m)}_{\mathrm{num}}(\mathbf{1}\theta), \boldsymbol{\phi}^{(n)}_{\mathrm{num}}(\mathbf{1})\right) = \frac{\left(\boldsymbol{\phi}^{(m)\mathrm{T}}_{\mathrm{num}}(\mathbf{1}\theta)\boldsymbol{\phi}^{(n)}_{\mathrm{num}}(\mathbf{1})\right)^2}{\left\|\boldsymbol{\phi}^{(m)}_{\mathrm{num}}(\mathbf{1}\theta)\right\|^2 \left\|\boldsymbol{\phi}^{(n)}_{\mathrm{num}}(\mathbf{1})\right\|^2}. \tag{26}$$

If a solid line that covers a dotted line shifts to overlay another dotted line, it indicates a change in the order of the matched numerical modes. The plot demonstrates that the matched numerical natural frequency may not depend monotonically on the index of the mode being matched. The mode switching effect is evident from the sudden changes in the matched natural frequencies. Some frequencies switch several times, as seen for $f^{\mathrm{num}}_8(\mathbf{1}\theta)$ and $f^{\mathrm{num}}_9(\mathbf{1}\theta)$. For some values of the θ parameter, several modes obtained for $\theta = 1$ can be matched to the same mode (overlapping solid lines) which leaves other modes unmatched (dotted-only lines). These observations emphasize the importance of careful matching of numerical and experimental modes when using the mode matching method.

For $\theta = 1$, the first five natural frequencies of the FE model are close to the corresponding measured values (Table 2). The order of the first five natural frequencies is the same as the measured ones, but the higher frequencies need to be matched before comparison. The natural frequencies are highly sensitive to the parameter θ near $\theta = 1$, except for the 7th and 8th frequencies. These properties suggest that the selected value of k_R is appropriate as the nominal value and $\boldsymbol{\theta}_0 = \mathbf{1}$ as the initial value of the unknown parameters.

Two parameterization methods are used. The first, simplified to two parameters, is shown in Fig. 10b and scales the rotational stiffness of all vertical and horizontal bolted connections by $\tilde{\theta}_1$ and $\tilde{\theta}_2$, respectively. This simplified procedure can be used for initial model updating before employing the fine parameterization shown in Fig. 10c, where one parameter is used per each bolted connection (totaling 16 parameters) and an additional parameter for scaling the stiffness of the beams. This allows for precise tuning of the model to measurement data.

3.2. Experimental modal analysis

Due to the uncertainties of the bolted connections, performing modal analysis in a broad frequency range proved challenging. To determine the optimal type and location of excitations and sensors required to reveal all vibration modes, an iterative modal identification procedure was performed. This involved alternating experimental measurements with numerical tests using increasingly accurate FE models. Successive iterations revealed the expected modes to be excited in the subsequent experiments. Table 1 summarizes the experiments, measured quantities, and methods. Modal data were extracted from measured signals using the stochastic subspace identification method with the aid of the LMS SCADAS system and LMS Test.Lab software.

The vibration modes identified in data sets #4 and #5 are inconsistent due to different excitations (impact-testing vs. modal shakers), so some of the vibration modes identified in data set #4 do not appear in #5, and vice versa. Additionally, the number of accelerometer locations increases in subsequent data sets. To obtain the final natural frequencies and mode shapes, all data must be synthesized. This also enables the estimation of variances for the modal parameters used in model updating and the calculation of uncertainties for the unknown parameters.

Table 1
Measured quantities and methods used in specific experiments.

Data set	Measured quantities	method
#1	First five natural frequencies (IP[a] only) measured with 18 sensor locations	Impact testing
#2	First eight natural frequencies, corresponding mode shapes and modal damping factors (IP[a] only), measured with 18 sensor locations	Impact testing – Roving Hammer
#3	First ten natural frequencies, corresponding mode shapes and modal damping factors (IP[a] only), measured with 27 sensor locations	Impact testing – Roving Hammer
#4	First 25 natural frequencies, corresponding mode shapes and modal damping factors (IP[a] and OoP[b], range: 0–1 kHz), measured with 41 sensor locations[c]	Impact testing – Roving Accelerometer
#5	From 6th to 24th natural frequencies, corresponding mode shapes and modal damping factors (IP[a] and OoP[b], range: 60–1000 Hz), measured with 41 sensor locations[c]	modal shakers – Roving Accelerometer

[a]IP: in-plane vibration modes.
[b]OoP: out-of-plane vibration modes.
[c]The data sets #4 and #5 are not fully consistent and contain several different identified mode shapes.

The vibration modes were identified in the frequency range from 0 to 1 kHz, including both in-plane (IP) and out-of-plane (OoP) modes. The focus is on the IP modes as the investigated frame was designed to examine and control IP vibrations. The average values and the CoVs of the natural frequencies of the IP modes, $\overline{f}_m$ and V_m^f, are listed in Table 2, along with the normalized standard deviation (NSD) of the mode shapes, S_m^{ψ}. The NSD is calculated as follows:

$$S_m^{\psi} = \frac{\overline{\sigma}_m^{\psi}}{\mathrm{RMS}\left(\hat{\boldsymbol{\psi}}^{(m)}\right)}, \tag{27}$$

where $\overline{\sigma}_m^{\psi}$ is the average standard deviation obtained as the mean of standard deviations of mth mode shape that are calculated at each sensor location from all available data sets. $\mathrm{RMS}\left(\hat{\boldsymbol{\psi}}^{(m)}\right)$ is calculated as $\mathrm{RMS}\left(\hat{\boldsymbol{\psi}}^{(m)}\right) = \sqrt{\frac{1}{N_\mathrm{o}}\sum_{s=1}^{N_\mathrm{o}} \hat{\psi}_s^{(m)2}}$, and $\hat{\psi}_s^{(m)}$ represents the mth measured mode shape at the sth sensor location, synthesized from all measurement sessions. To find the averaged mode shape and $\overline{\sigma}_m^{\psi}$, vibration modes from different data sets were scaled to the mode shapes from data set #5 (or data set #4 for modes missing in #5) using the modal scale factor c_m defined in Eq. (7). The modal scale factor was calculated using only the sensor locations common for the two vectors.

The average standard deviation $\overline{\sigma}_m^{\psi}$ is used to reconstruct the covariance matrix $\boldsymbol{\Sigma}_\mathrm{M}$, Eq. (8). The diagonal block $\boldsymbol{\Sigma}_m$ of $\boldsymbol{\Sigma}_\mathrm{M}$ that corresponds to the mth mode shape is calculated as follows:

$$\boldsymbol{\Sigma}_m = (\overline{\sigma}_m^{\psi})^2 \mathbf{I}_{N_\mathrm{o}\times N_\mathrm{o}} = \left[\mathrm{RMS}\left(\hat{\boldsymbol{\psi}}^{(m)}\right) S_m^{\psi}\right]^2 \mathbf{I}_{N_\mathrm{o}\times N_\mathrm{o}}, \tag{28}$$

where $\mathbf{I}_{N_\mathrm{o}\times N_\mathrm{o}}$ is the identity matrix of appropriate dimensions. In Eq. (28), the NSD is expanded to encompass all sensor locations instead of calculating it independently for each specific sensor location. This approach is adopted due to the limited number of measurement sessions (up to four, as in data set #1 only natural frequencies were measured) and due to the varying number of sensor locations in different data sets. Moreover, covariance matrices estimated in this manner result in better conditioning of the optimization problems described in Sections 2.2 and 2.3.

The CoVs for natural frequencies, shown in Table 2, have small values close to 1%. This is due to the accurate measurement of the natural frequencies. The differences between the different data sets may arise from the long time intervals between measurement sessions and the fact that the structure was disassembled and reassembled once. The CoV maintains a relatively constant trend for subsequent natural frequencies: the larger the measured natural frequency, the larger its variance. The NSD values for the mode shapes are greater by approximately one order of magnitude, as the measurement of mode shapes is less accurate. The NSD exhibits an increasing trend with the mode order, similar to the standard deviation of natural frequencies, consistent with the constant trend of the CoV. For some frequencies only two measurements are available, and thus the CoV may be calculated with a significant uncertainty.

The power spectral density function (PSD) for three impact points, along with the IP mode shapes and natural frequencies of the OoP modes, is shown in Fig. 11. Some peaks of the PSD plot are not as distinguishable as others due to the reduced controllability of particular modes by external forces, corresponding to the limited displacement of the mode shape at impact locations or directions (e.g., OoP modes), see top-right corner of Fig. 11. IP mode shapes without a pronounced PSD peak have nodes close to the impact

Table 2
Statistical metrics for the measured natural frequencies and mode shapes from all datasets.

IP mode	Selected	Freq. f_n [Hz] for each dataset					Mean	CoV[a]	NSD[b]
m_{2D} [−]	m [−]	#1	#2	#3	#4	#5	$\overline{f}_m$ [Hz]	V_m^f [%]	S_m^Ψ [%]
1	1	9.39	9.49	9.46	9.23	–	9.39	1.24	5.22
2	2	30.41	30.60	30.50	30.54	–	30.51	0.26	5.63
3	3	70.40	71.55	71.55	70.98	72.52	71.40	1.10	4.70
4	4	228.84	228.99	229.11	225.51	225.85	227.66	0.80	7.67
5	5	250.18	250.40	250.39	247.89	247.72	249.32	0.55	11.56
6	–	–	324.66	328.60	–	324.68	325.98	0.70	22.23
7	–	–	335.95	–	338.92	338.88	337.92	0.50	8.91
8	–	–	–	369.92	363.50	–	366.71	1.24	80.77
9	6	–	–	427.81	424.17	430.57	427.51	0.75	27.23
10	–	–	–	500.44	499.75	–	500.09	0.10	42.95
11	7	–	–	–	572.17	591.12	581.64	2.30	14.47
12	8	–	–	–	768.83	763.60	766.22	0.48	13.57
13	9	–	–	–	830.41	821.71	826.06	0.75	22.03
14	–	–	–	–	–	886.99	886.99	–	–
15	–	–	–	–	955.52	–	955.52	–	–

[a]Coefficient of variation.
[b]Normalized standard deviation for corresponding mode shapes.

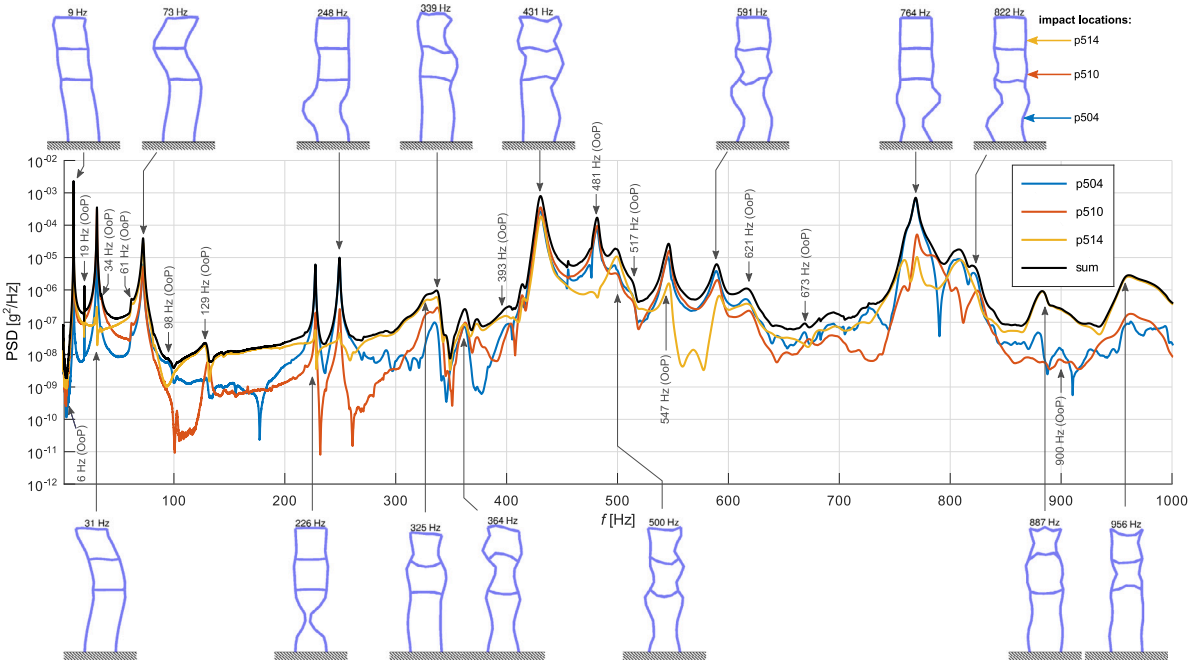

Fig. 11. Power spectral density function (PSD) for three impact points with marked identified IP modes and natural frequencies of OoP modes. Impact locations are illustrated in the top-right corner of the figure.

locations. However, there are three IP modes (325 Hz, 339 Hz, and 365 Hz) that should be well excited by at least one impact, but their PSD peaks are not distinctive and have values lower by one or more orders of magnitude than those of the other IP modes, including higher-order modes. Based on the contribution of the vibration modes to the PSD function, only the IP vibration modes 1–5, 9, 11–13 were selected for model updating. Their numbering is shown in the second column of Table 2.

It is an important observation that many mode shapes display significant asymmetries and other shape deviations, which is due to discrepancies in the assembly of the bolted connections. This indicates that the parameters of the bolted connections are highly uncertain.

4. Rotational stiffness identification using experimental data

The methods discussed in Section 2 are used to identify the parameters of the bolted connections in the laboratory-scale structure described in Section 3. Whenever necessary, numerical modes are matched to the mth experimental mode using the following

criterion:

$$k_m = \arg\max_k \left[\mathrm{MAC}\left(\hat{\boldsymbol{\psi}}^{(m)}, \boldsymbol{\phi}_{\mathrm{num}}^{(k)}(\boldsymbol{\theta})\right)\right]. \tag{29}$$

For notational simplicity, the index k_m of the matched numerical mode is replaced in this section with the number m of the experimental mode it is matched to.

4.1. Estimation based on mode matching

The FE model with the fine parameterization shown in Fig. 10c is employed for model updating based on mode matching without using the preliminary crude parameterization (Fig. 10b). This is due to the numerical stability of the method. A value of $\kappa_\theta = 0.3$ was selected by trial-and-error as it resulted in a fast convergence of the algorithm (Eq. (20)). The stop condition is that for all components θ_l of the vector $\boldsymbol{\theta}$, the absolute value of the relative increment $\frac{|\Delta\theta_l|}{\theta_l}$ must be below 10^{-5}. The initial values for all unknown parameters are set equal to one. The weighting matrix is reciprocal to the measurement covariance matrix (Eq. (8)), which is selected so that it corresponds to the data presented in Table 2.

The results are depicted in Fig. 12. The relative error between the numerical and measured natural frequencies converges to nearly zero. The frequency errors decreased from the highest value of almost 40% (for the second mode) to below 5% for all modes (Fig. 12d). The MAC between the measured and numerical mode shapes increased to almost one (above 0.9 for all modes), whereas before model updating, the lowest MAC value was below 0.5 (Fig. 12e).

A precise reproduction of structural dynamics was achieved with a significant dispersion in the identified parameters. The parameters identified for the bolted connections on the left-hand side of the structure (Fig. 12a) differ from those on the right-hand side (Fig. 12b), indicating that assembly discrepancies may be related to deviations in mode shapes. The parameter related to the Young's modulus of the beam material decreases during optimization, although its change is not as significant as that of the parameters related to the bolted connections. This is in agreement with engineering practice, as the uncertainty in Young's modulus is usually much lower than that of a bolted connection, where many local effects can influence the actual stiffness.

Regarding mode switching effect, the indices k_m of the numerical modes matched to the measured modes are plotted in Fig. 13. At the beginning of the model updating procedure, the 12th numerical vibration mode is matched to both the sixth and seventh experimental vibration modes. In the first iteration, this vibration mode is thus doubled in Eq. (18) and further calculations. In subsequent iteration steps, the 11th and 13th numerical vibration modes are matched with the sixth and seventh experimental ones, respectively. From the second iteration step the numerical modes do not change their matching order. These changes in mode order result in a small increase in the error of the seventh natural frequency (Fig. 12d) and a decrease of the MAC between the sixth measured mode shape and the matched numerical shape (Fig. 12e) in the second iteration. The mode-switching effect occurs only once, and it does not induce any numerical instability or diminish the quality of the model updating procedure. Results in shown in Fig. 13 indicate that the MAC criterion can correctly match modes even for wide-band frequency modal data. It is related to the relatively dense sensor network.

A comparison between the numerical mode shapes, $\boldsymbol{\phi}_{\mathrm{num}}^{(m)}(\boldsymbol{\theta})$, calculated for the final value of $\boldsymbol{\theta}$ and the measured mode shapes is presented in Fig. 14 (left-hand side of each subfigure). Additionally, the numerical mode shapes calculated for the ideally rigid connections, $\boldsymbol{\phi}_{\mathrm{r}}^{(m)}$, are also compared with the measured mode shapes, $\hat{\boldsymbol{\psi}}^{(m)}$, as shown in the right-hand side of each subfigure. It is evident that the independent parameterization of the bolted connections enables fitting the model to even highly asymmetric mode shapes. In contrast to the numerical mode shapes of the updated model, $\boldsymbol{\phi}_{\mathrm{num}}^{(m)}(\boldsymbol{\theta})$, the mode shapes $\boldsymbol{\phi}_{\mathrm{r}}^{(m)}$ are significantly different from the measured ones. The corresponding numerical natural frequencies, f_m^{r}, are also greater by 20%–150% compared to the updated numerical frequencies.

An inspection of Fig. 12a and the sixth vibration mode depicted in Fig. 14f reveals that a near right angle between the bottom horizontal beam and the connected beams on the left-side corresponds to a high stiffness of the bolted connections parameterized by θ_2 and θ_{11}. The high values of these parameters are also consistent with the fact that the mode shape shown in Fig. 14i, which mostly involves the vibration of the beams connected to the bottom-left joint, has the highest natural frequency $f_9^{\mathrm{num}}(\boldsymbol{\theta}) = 818.81$ Hz.

4.2. Estimation using the Bayesian approach

This subsection discusses the Bayesian framework for parametric identification. To leverage the key property of the MAP formulation, which considers both measurement and modeling errors, special attention is given to the selection of the parameter σ_C in Eq. (14).

To facilitate the convergence, the Bayesian updating procedure is divided into two stages:

Stage I The simplified parameterization is used (Fig. 10b) and only the first five modes are considered. The initial parameters for the iterative algorithm are set as $\widetilde{\boldsymbol{\theta}}_0 = \begin{bmatrix}1 & 1\end{bmatrix}^{\mathrm{T}}$.

Stage II All selected measured vibration modes, $m = 1, 2, \ldots, 9$ (as listed in Table 2), are used and the independent parameterization of each bolted connection and the Young's modulus of the beams is adopted (Fig. 10c). The initial parameters for the iterative algorithm, $\boldsymbol{\theta}_0 = \begin{bmatrix}\theta_{01} & \theta_{02} & \cdots & \theta_{017}\end{bmatrix}^{\mathrm{T}}$, are equal to the final values of the corresponding parameters updated in Stage I: for the vertical beams, $\theta_{01} = \theta_{02} = \cdots = \theta_{010} = \widetilde{\theta}_1$; for the horizontal beams, $\theta_{011} = \theta_{012} = \cdots = \theta_{016} = \widetilde{\theta}_2$; and the additional parameter introduced at this stage, $\theta_{017} = 1$.

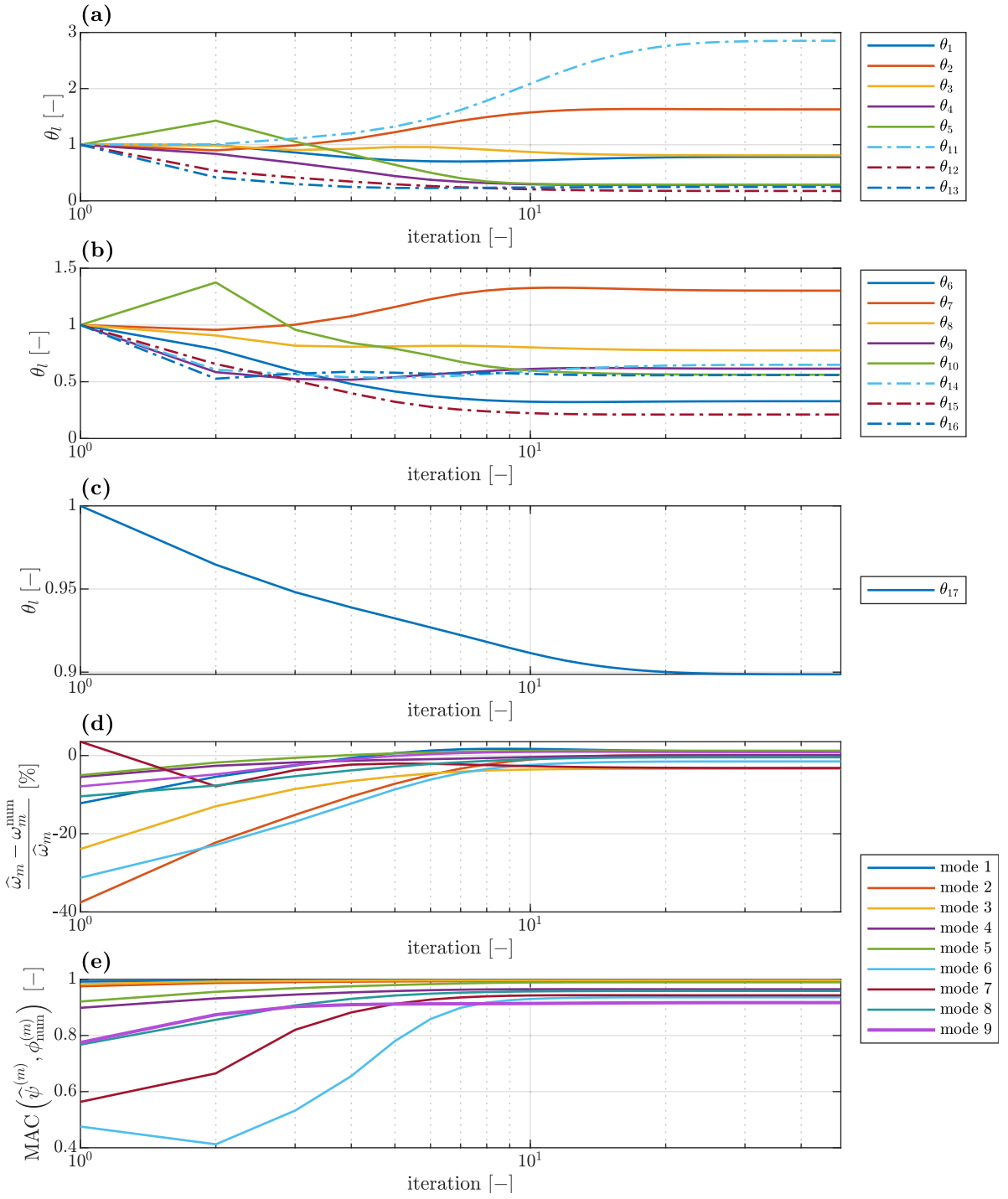

Fig. 12. Evolution of parameters in model updating based on mode matching: (a) stiffness parameters of the bolted connections on the left hand side of the structure, (b) stiffness parameters of the bolted connections on the right hand side of the structure, (c) stiffness parameter of the beams, (d) relative frequency error, and (e) MAC between the measured and numerical mode shapes.

The assumption is that the reduced parameterization employed in Stage I provides the values of the parameters around which the optimal parameters determined in Stage II are scattered. This division of the updating process helps to avoid local minima of the objective function.

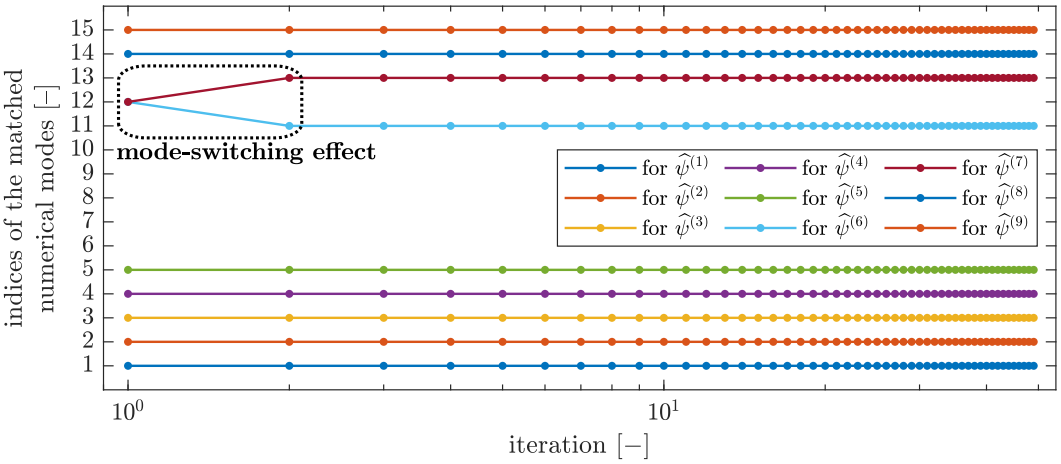

Fig. 13. Indices k_m of the numerical modes matched with the experimental modes during subsequent iterations of the mode matching method.

The covariance matrix of the measurement errors, $\boldsymbol{\Sigma}_{\mathrm{M}}$, is identical to that used in the mode matching procedure. The remaining weights need to be chosen. Following the recommendations of the authors of the method [23], $\boldsymbol{\Sigma}_{\theta}$, which represents the expected covariance matrix of the unknown parameters, is selected to have large values: $\boldsymbol{\Sigma}_{\theta} = 4.4 \cdot 10^{26} \cdot \mathbf{I}_{N_\theta \times N_\theta}$ for Stage I and $\boldsymbol{\Sigma}_{\theta} = 8.1 \cdot 10^{28} \cdot \mathbf{I}_{N_\theta \times N_\theta}$ for Stage II. Larger values are chosen for Stage II because the matrices are proportional to the average measurement error variances which differ between Stage I and II. Large values of $\boldsymbol{\Sigma}_{\theta}$ model the absence of prior knowledge about the parameters. The stop condition in both stages is that, for all components θ_l of the vector $\boldsymbol{\theta}$, the absolute value of the increment $|\Delta\theta_l|$ is less than 10^{-9}. The required increment has a much lower value than that used in mode matching model updating due to the slower convergence of the Bayesian method.

Finally, the parameter σ_C, which represents the expected modeling errors, must be selected. As discussed in Sections 2.3 and 2.7, if σ_C is too small, λ_m and $\boldsymbol{\phi}^{(m)}$ will remain close to their numerical counterparts, and the FE model $(\mathbf{M}, \mathbf{K}(\boldsymbol{\theta}))$ will not change during the model updating, as it will be treated as more reliable than the measurements. Conversely, if σ_C is too large, λ_m and $\boldsymbol{\phi}^{(m)}$ can fit too strongly to the measurement data, thereby also reproducing measurement noise. It is thus recommended to initially select a small value of σ_C. If an appropriate trade-off between measurement and modeling errors is not achieved, then σ_C should be increased.

Taking into account the above considerations, a parametric study was performed for Stage I. The model updating procedure was performed for different values of σ_C. The results are shown in Fig. 15. Due to the significant computational effort required to update the model for each particular σ_C, the maximum number of iterations was limited to 15,000. This limitation does not apply to other results. Figs. 15b and 15c reveal that, as σ_C increases, the modeling error for the updated model also increases, and the error between the most probable modal and measured data decreases. This is in agreement with the considerations above and in Section 2.7.

According to the recommendations of the authors of the method [23], the value of $\sigma_C^{\mathrm{I}} = 10^4$ was selected for Stage I as it results in the most probable mode shapes $\boldsymbol{\phi}^{(m)}$ being well-fitted to the measured mode shapes, including their asymmetry, but still avoiding reproduction of measurement noise. This is evident in Fig. 16, which depicts the most probable vibration modes obtained for the selected value of σ_C^{I}. Due to the reduced parameterization (Fig. 10b), the numerical mode shapes $\boldsymbol{\phi}_{\mathrm{num}}^{(m)}(\boldsymbol{\theta})$, obtained from the updated FE model, cannot reproduce the asymmetry of the structure, unlike the most probable mode shapes $\boldsymbol{\phi}^{(m)}$.

It is clear that the selected value of σ_C^{I} results in an appropriate balance between measurement and modeling errors. This is demonstrated by the fact that both $\mathbf{e}_C^{\mathrm{T}}\mathbf{e}_C$ and $\mathbf{e}_{\mathrm{M}}^{\mathrm{T}}\boldsymbol{\Sigma}_{\mathrm{M}}^{-1}\mathbf{e}_{\mathrm{M}}$ are far from their maximum values. Moreover, the metric ε, which measures the error between the numerical and measured modal data, reaches a near-minimum value at $\sigma_C = \sigma_C^{\mathrm{I}}$, despite the fact that it was not considered during the selection of σ_C^{I}.

Fig. 17 shows the evolution of unknown parameters, natural frequency errors, and MAC values for the selected σ_C^{I}. Fig. 17b displays the relative error between numerical and measured natural frequencies (solid lines), and the measured and most probable values (dashed lines). The most probable frequencies tend to converge to the numerical values, while both simultaneously converge to the measured values. This is particularly visible for the third mode. However, the first and second numerical natural frequencies, unlike the corresponding most probable frequencies, do not converge properly to the measured values. This can be attributed to the systematic error (bias) related to the reduced parameterization of the FE model.

The Bayesian approach requires approximately $2 \cdot 10^5$ iterations to complete the model updating process in Stage I. The slow convergence may be attributed to the division of each iteration step into three sub-steps and the subsequent minimization of the objective function with respect to the variables $\boldsymbol{\lambda}$, $\boldsymbol{\phi}$, and $\boldsymbol{\theta}$. Similar difficulties are observed in the illustrative example with an underestimated Young's modulus of the beams, as depicted in Fig. 7d.

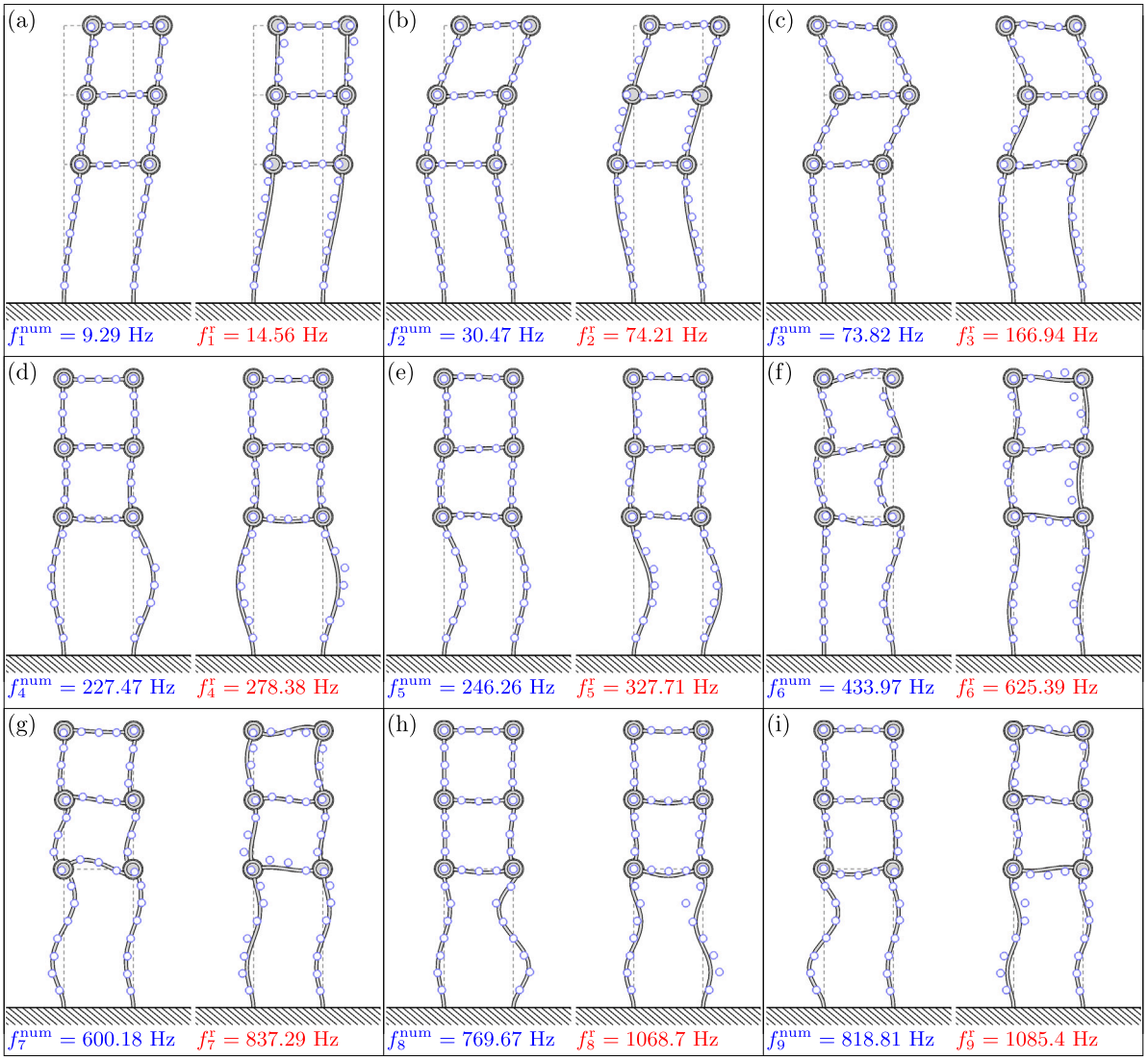

Fig. 14. Comparison of numerical mode shapes $\boldsymbol{\phi}_{\mathrm{num}}^{(m)}(\boldsymbol{\theta})$ obtained with the mode matching method (solid lines) and measured mode shapes $\hat{\boldsymbol{\psi}}^{(m)}$ (blue points at sensor locations), together with an analogous comparison obtained for FE model with bolted connections assumed to be ideally rigid.

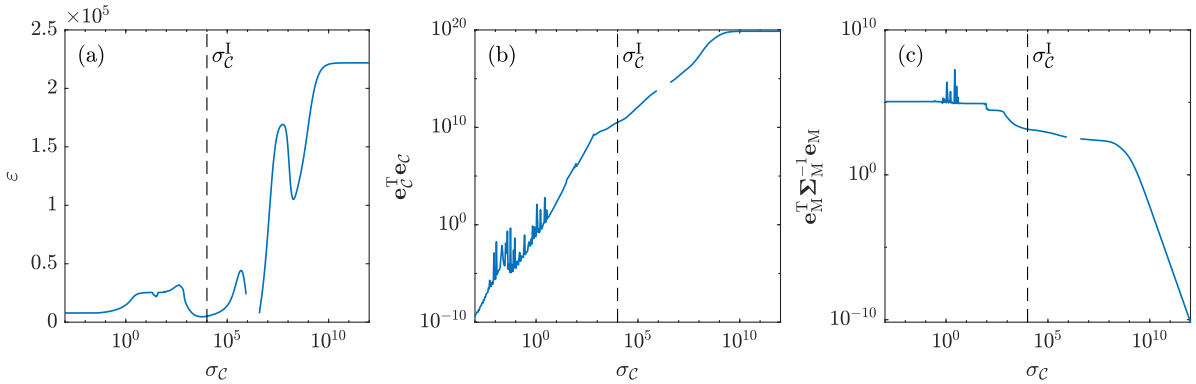

Fig. 15. Dependence of various error metrics in the Bayesian approach on the parameter $\sigma_{\mathcal{C}}$ for Stage I: (a) weighted norm ϵ of the differences between numerical and measured modal data, (b) modeling error $\mathbf{e}_{\mathcal{C}}^{\mathrm{T}}\mathbf{e}_{\mathcal{C}}$, and (c) measurement error weighted with respect to its reciprocal covariance matrix $\mathbf{e}_{\mathrm{M}}^{\mathrm{T}}\boldsymbol{\Sigma}_{\mathrm{M}}^{-1}\mathbf{e}_{\mathrm{M}}$.

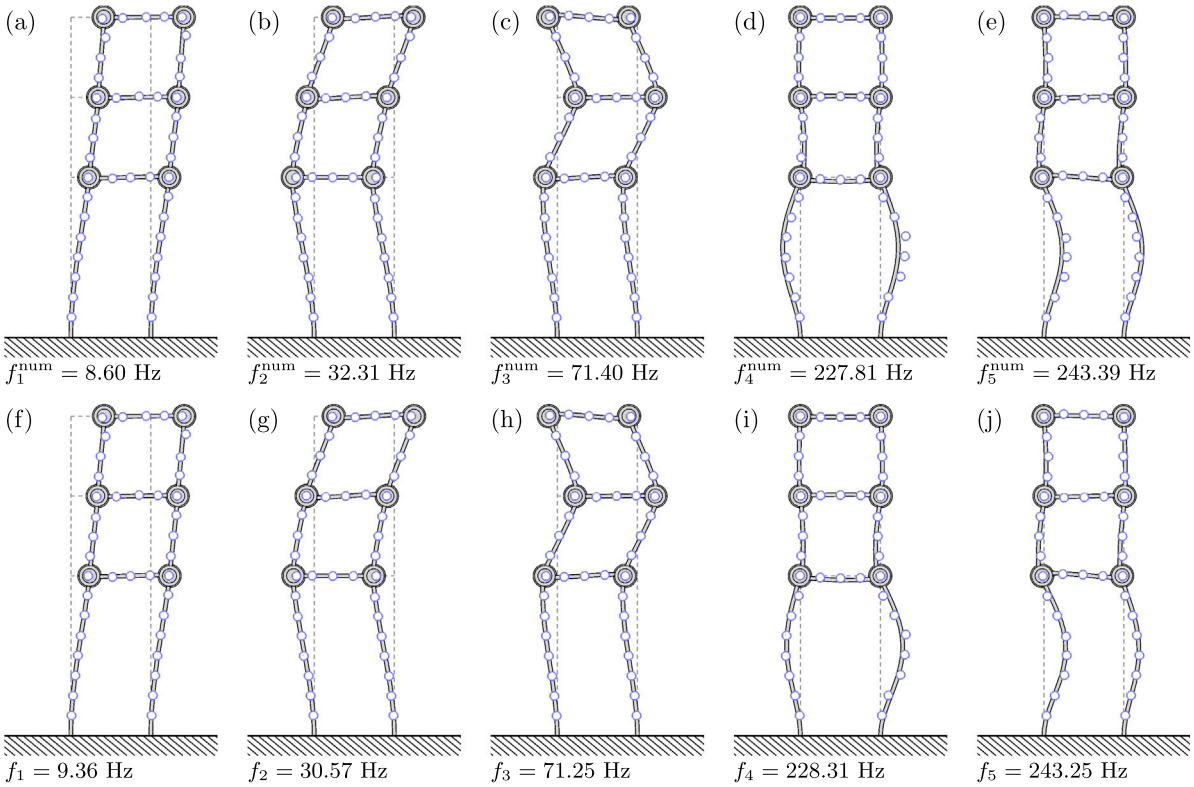

Fig. 16. Numerical mode shapes $\boldsymbol{\phi}_{\text{num}}^{(m)}(\boldsymbol{\theta})$ (a–e) and the most probable system mode shapes $\boldsymbol{\phi}^{(m)}$ (f–j) (solid lines) obtained in Stage I of Bayesian model updating for $\sigma_C = \sigma_C^{\text{I}}$, compared with the measured mode shapes $\hat{\boldsymbol{\psi}}^{(m)}$ (blue points at sensor locations).

The MAC values between the measured and most probable mode shapes, and the measured and numerical mode shapes, remain relatively constant (Fig. 17c). The MAC values calculated for the most probable shapes are higher than those for the numerical shapes due to a closer reproduction of the measured mode shapes. This can be observed by comparing Figs. 16a–e and f–j.

In order to select an appropriate value for σ_C in Stage II, a similar analysis as in Stage I was performed. The results are shown in Fig. 18. The value of $\sigma_C^{\text{II}} = 9 \cdot 10^4$ was selected through trial-and-error to fit the most probable modal data to the measured data. As shown in Fig. 18c, this value is just behind a small step-like decrease of the measurement error metric. This sudden decrease corresponds to the value of σ_C below which not all most probable mode shapes are yet well correlated with the measured mode shapes. Similar to Stage I, the selected value of σ_C^{II} results in both the modeling and measurement errors being far from their maximum values (see Figs. 18b and 18c, respectively). Once again, the error between the numerical and measured modal data is close to its minimum value, despite not being used during the selection of σ_C^{II}.

The evolution of the unknown parameters and the error metrics for $\sigma_C = \sigma_C^{\text{II}}$ is shown in Fig. 19. The third and seventh numerical natural frequencies exhibit the largest errors at the final iterations (Fig. 19d). The most probable third natural frequency remains close to the measured value, while the seventh converges to the numerical value. This suggests that the selected class of models is unlikely to accurately reproduce the third natural frequency and that the seventh numerical frequency is more reliable than the measured one.

Similar as in Stage I, the convergence is slow ($5 \cdot 10^5$ iterations). As with the mode matching approach, the parameters related to the bolted connections on the right-hand side of the structure differ from those on the left-hand side and are strongly dispersed. The parameter θ_{17} (Young's modulus of the beams) does not change as significantly as the other unknown parameters.

The MAC values for the numerical mode shapes are similar to those obtained using the mode matching approach and attain an acceptable level. The most probable shapes are closer to the measured ones than the numerical shapes, thus their corresponding MAC values are also closer to one. Both the numerical and the most probable mode shapes are very similar to the numerical mode shapes obtained using the mode matching approach and, therefore, they are not shown here.

4.3. Comparison of identification results

Values of θ_l, $l = 1, 2, \ldots, 17$, obtained through mode matching and the Bayesian model updating approach are compared in Fig. 20. The horizontal lines represent the mean values, $\overline{\theta}_{\text{v}}$ and $\overline{\theta}_{\text{h}}$, calculated for all vertical (θ_1 to θ_{10}) and horizontal (θ_{11} to θ_{16})

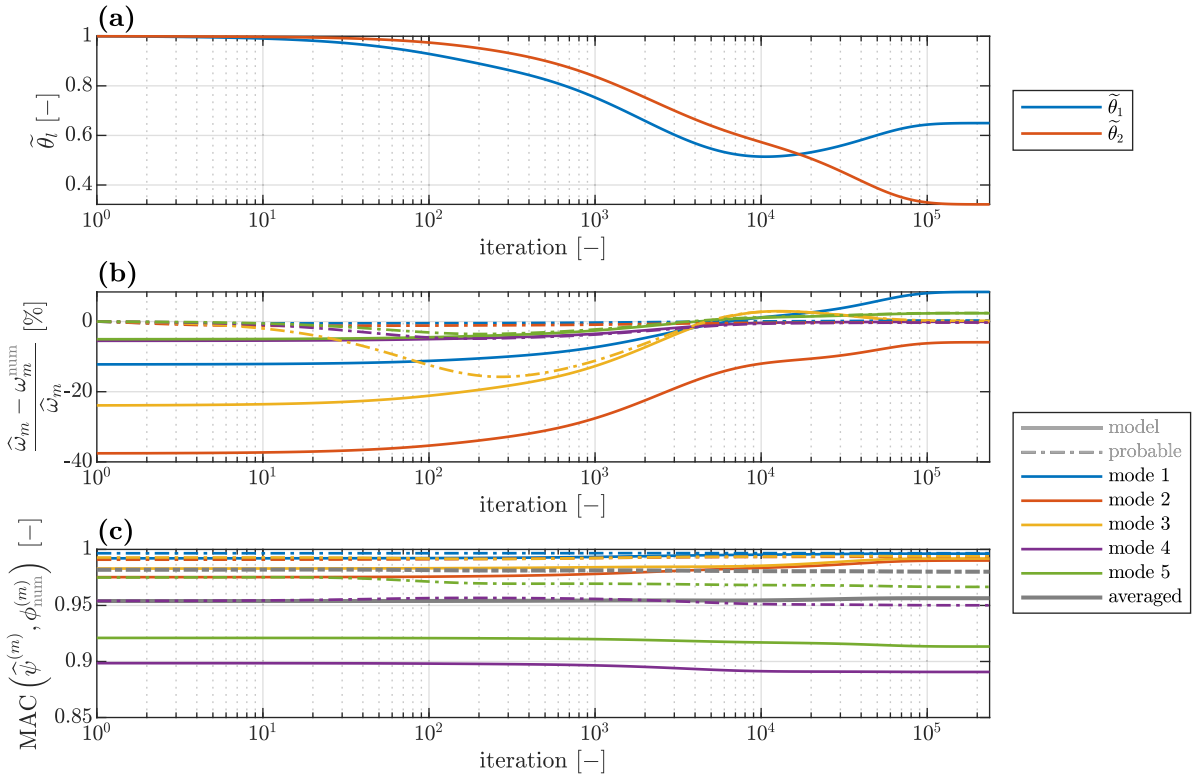

Fig. 17. Evolution of parameters in Stage I of Bayesian model updating for $\sigma_c = \sigma_c^{\text{I}}$: (a) unknown parameters, (b) relative frequency error for numerical natural frequencies (solid lines) and the most probable natural frequencies (dashed lines), (c) MAC between the measured and numerical mode shapes (solid lines) and between the measured and the most probable mode shapes (dashed lines).

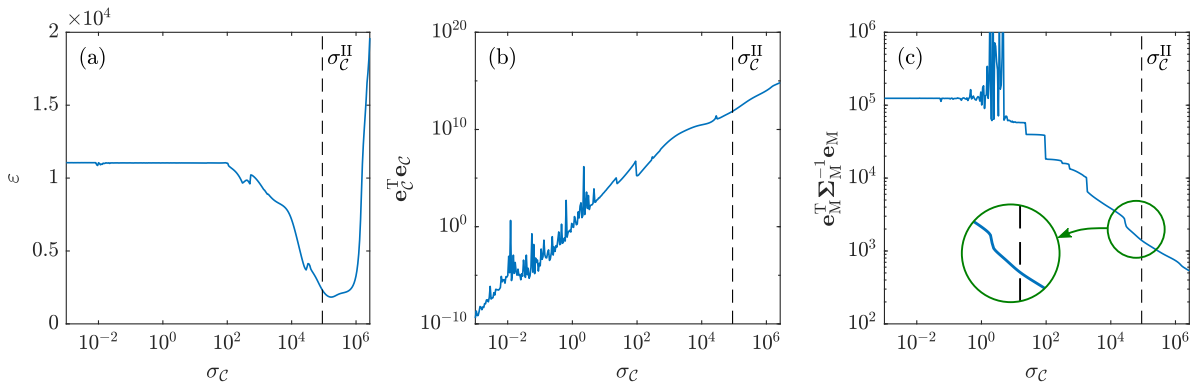

Fig. 18. Dependence of various error metrics obtained with the Bayesian approach on σ_c for Stage II: (a) weighted norm of the differences between the numerical and measured modal data ε, (b) modeling error $\mathbf{e}_C^{\text{T}}\mathbf{e}_C$, and (c) measurement error weighted with respect to its reciprocal covariance matrix $\mathbf{e}_{\text{M}}^{\text{T}}\boldsymbol{\Sigma}_{\text{M}}^{-1}\mathbf{e}_{\text{M}}$.

bolted connections, respectively. The significant dispersion of the parameters for both methods is due to assembly discrepancies and indicates the uncertainty of such bolted connections.

A comparison of $\overline{\theta}_{\text{v}}$ and $\overline{\theta}_{\text{h}}$ with the corresponding parameters $\widetilde{\theta}_1$ and $\widetilde{\theta}_2$ obtained in Stage I of Bayesian model updating (Fig. 17a) shows that $\widetilde{\theta}_1$ and $\widetilde{\theta}_2$ are not equal to the mean values of the respective parameters θ_l. This is due to the nonlinearities in the eigenvalue equation with respect to $\boldsymbol{\theta}$ (Fig. 9b). High values of θ_l cause the bolted connections to behave more like semi-rigid nodes, and for stiffer bolted connections, the modal data is less sensitive to changes in the stiffness parameters. As a result, directly calculating the mean of the parameters can overestimate the common value obtained through reduced parameterization.

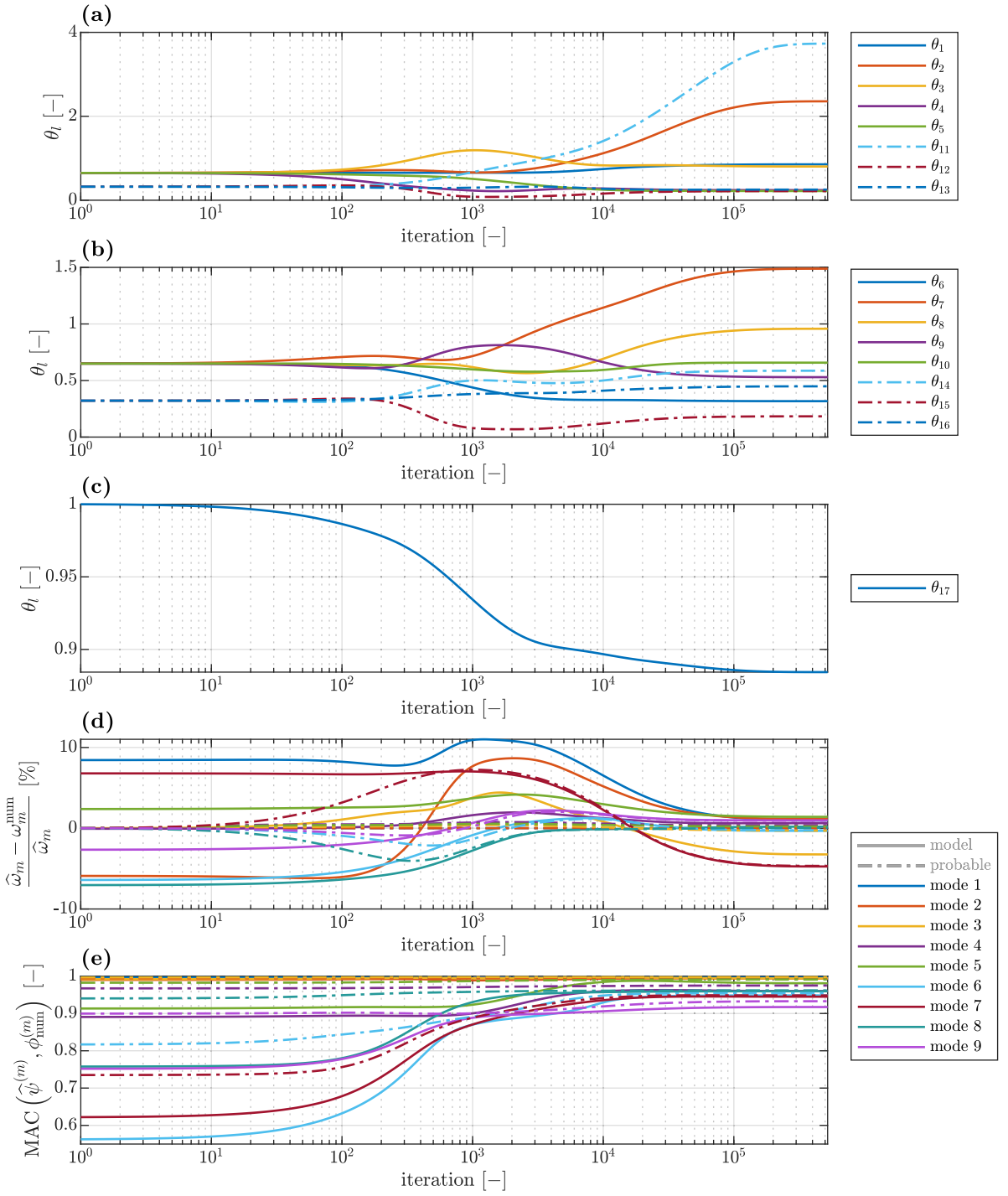

Fig. 19. Evolution of parameters in Stage II of Bayesian model updating for $\sigma_c = \sigma_c^{\text{II}}$: (a) stiffness parameters of the bolted connections on the left-hand side of the structure and on the (b) right-hand side of the structure, (c) stiffness parameter of the beams, (d) relative frequency errors for the numerical natural frequencies (solid lines) and the most probable natural frequencies (dashed lines), (e) MAC between the measured and numerical mode shapes (solid lines) and between the measured and the most probable mode shapes (dashed lines).

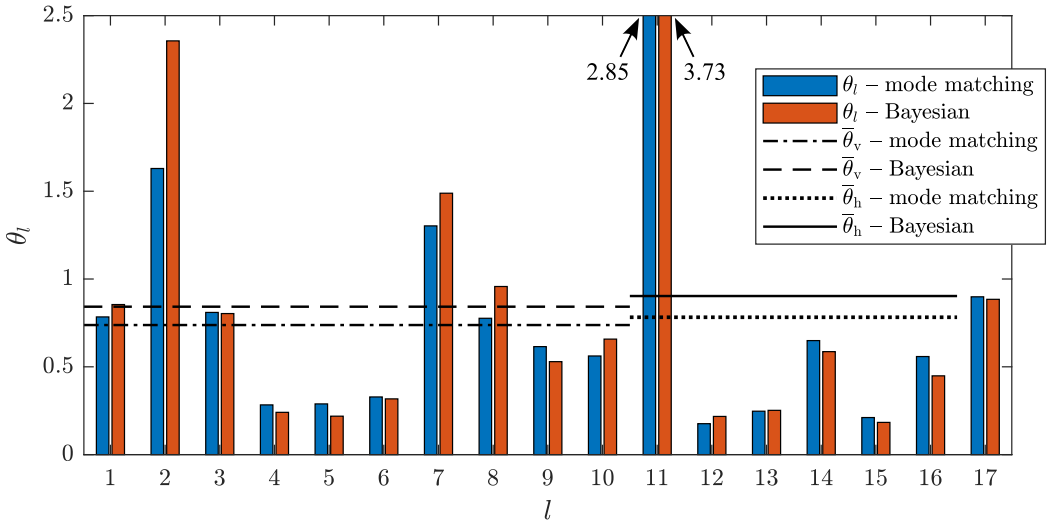

Fig. 20. Comparison of the unknown parameters obtained using independent parameterization of each bolted connection with both the mode matching approach and the Bayesian approach, together with the corresponding mean values for the vertical and horizontal bolted connections.

Table 3
Comparison of results obtained with the mode matching and Bayesian approach.

Method	Coefficient of variation, Eq. (30)		Weighted square error, Eq. (5)	Number of iterations
	$\widehat{V}_\theta^\mathrm{v}$ [%]	$\widehat{V}_\theta^\mathrm{h}$ [%]	ε [–]	
Mode matching	59.67	131.96	1591.5	50
Bayesian	77.97	154.35	1797.25	$2 \cdot 10^5 + 5 \cdot 10^5$

The comparison of the parameters obtained using both methods shows a good agreement, with the exception of parameters related to the very stiff bolted connections, i.e. θ_2 and θ_{11} (Fig. 20). Table 3 summarizes the selected properties of the results obtained from both methods. It is evident that the CoVs calculated for all vertical bolted connections and all horizontal ones,

$$\widehat{V}_\theta^\mathrm{v} = \frac{\sqrt{\frac{1}{15}\sum_{l=1}^{10}\left(\theta_l - \overline{\theta}_\mathrm{v}\right)^2}}{\overline{\theta}_\mathrm{v}}, \quad \widehat{V}_\theta^\mathrm{h} = \frac{\sqrt{\frac{1}{5}\sum_{l=11}^{16}\left(\theta_l - \overline{\theta}_\mathrm{h}\right)^2}}{\overline{\theta}_\mathrm{h}}, \tag{30}$$

respectively, have different values for each method. The mode matching approach results in a smaller scatter of the parameters and a lower error metric ε (Eq. (5)).

In terms of computational efficiency, the mode matching method outperforms the Bayesian approach. The mode matching method requires only 50 iterations, while the Bayesian approach requires approximately $7 \cdot 10^5$ iterations, performed in two stages.

4.4. Uncertainties of the identified parameters

The identified parameters are not only characterized by their expected values, but also by their uncertainties, which are quantified by the covariance matrix. For the parameters estimated using the mode matching method, it was calculated as per Eq. (15). The standard deviations and the CoVs are presented in Fig. 21. The large standard deviations of the 11th, and to a lesser extent 2nd, parameter can be attributed to the differences in their values as obtained from the mode matching and Bayesian approaches (Fig. 20). The uncertainty of the 17th unknown parameter is the smallest due to the fact that this parameter scales the Young's modulus of the beams. The CoVs for the parameters related to the bolted connections are around 10%, which is a relatively high value. This can be attributed to the complex parameterization of the FE model. As the number of unknown parameters increases, the systematic error (bias) decreases, but this comes at the cost of a higher variance, which is known as the bias–variance trade-off.

In the Bayesian approach, the covariance matrix $\widehat{\boldsymbol{\Sigma}}_{\lambda\phi\theta}$ cannot be calculated as direct inverse of the Hessian matrix $\mathbf{H}$ (Eq. (16)) due to its ill-conditioning (the condition number of $\mathbf{H}$ is $1.5 \cdot 10^{15}$). The covariance matrix was thus calculated using the TSVD regularization and the L-curve technique, as described in Section 2.7. Fig. 22a presents the L-curve plot, that is, the dependence of the Frobenius norm of the calculated covariance matrix $\left\|\widetilde{\boldsymbol{\Sigma}}_{\lambda\phi\theta}(s_\mathrm{tol})\right\|_\mathrm{F}$ on the error $E(s_\mathrm{tol})$ defined in Eq. (25). Fig. 22b focuses on the vicinity of the selected singular value threshold. The solutions that exhibit negative values of variances on the diagonal of $\widetilde{\boldsymbol{\Sigma}}_{\lambda\phi\theta}(s_\mathrm{tol})$ are indicated by red dots. The spectrum of singular values is depicted in Fig. 22c. The singular values decrease rapidly below $s_\mathrm{tol} = 0.0010756$, which was selected as the threshold for the calculation of the regularized covariance matrix $\widetilde{\boldsymbol{\Sigma}}_{\lambda\phi\theta}(s_\mathrm{tol})$. This threshold value corresponds to the smooth corner of the L-curve plotted a lin–lin scale, as seen in Fig. 22b.

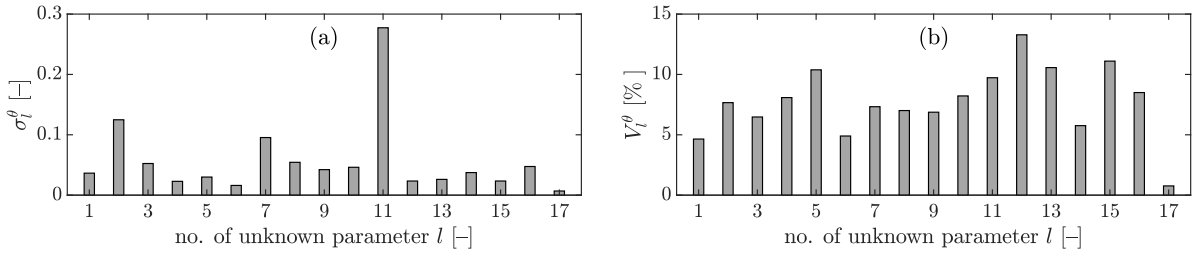

Fig. 21. Uncertainties of the unknown parameters θ_l estimated with the mode matching approach: (a) standard deviations and (b) coefficients of variation (CoVs).

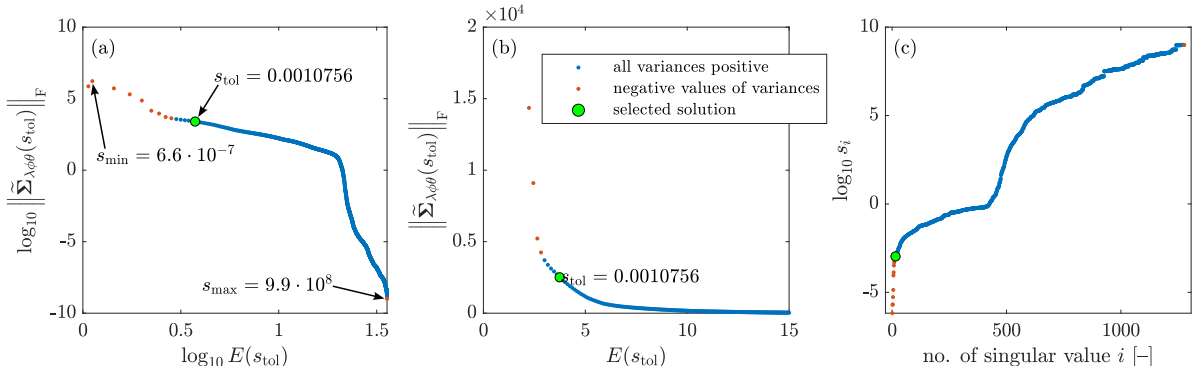

Fig. 22. Regularization of the covariance matrix $\widetilde{\boldsymbol{\Sigma}}_{\lambda\phi\theta}(s_{\text{tol}})$: (a) L-curve with indicated selected s_{tol}, (b) L-curve in the region around the selected s_{tol}, shown in a lin–lin scale, and (c) spectrum of singular values s_i for the matrix **H**.

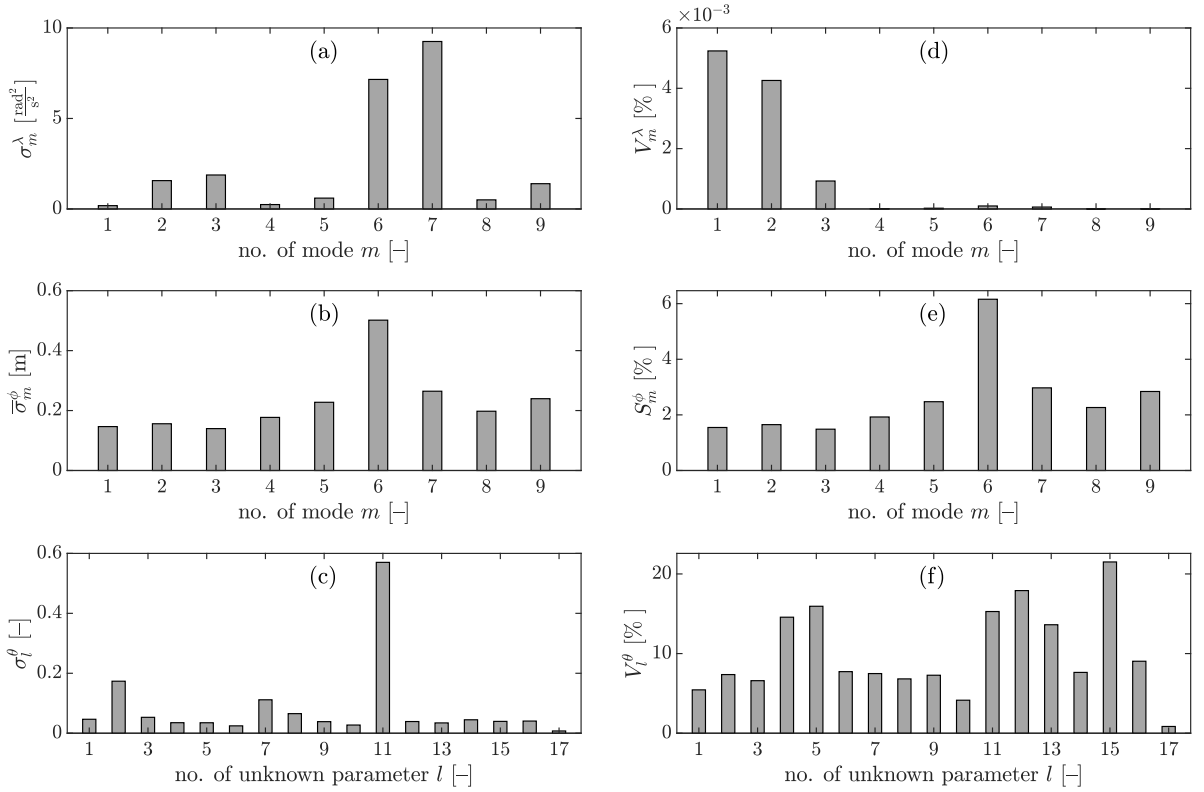

Fig. 23. Uncertainties of the most probable parameters for the Bayesian approach (Stage II) obtained with the TSVD regularization: (a) standard deviations of the eigenvalues λ_m, (b) mean standard deviations of the mode shapes calculated from all DOFs of each mode shape $\boldsymbol{\phi}^{(m)}$, (c) standard deviations of the unknown parameters θ_l, (d) CoVs of the eigenvalues λ_m, (e) normalized standard deviation of the mode shapes $\boldsymbol{\phi}^{(m)}$, and (f) CoVs of the unknown parameters θ_l.

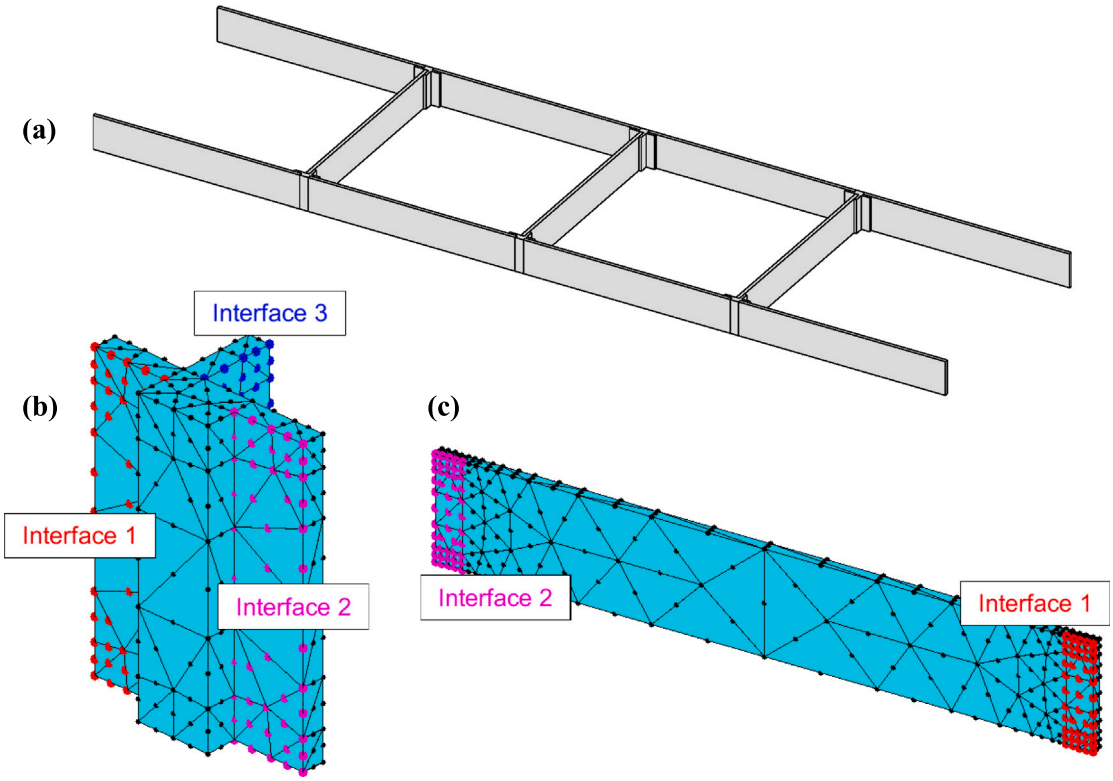

Fig. 24. Four-bay frame FE model: (a) model geometry, (b) FE mesh of the coupler, and (c) FE mesh of the beam.

The uncertainties obtained from the diagonal of $\widetilde{\boldsymbol{\Sigma}}_{\lambda\phi\theta}(s_{\text{tol}})$ for the selected s_{tol} are shown in Fig. 23. Fig. 23b depicts the mean standard deviations of all DOFs of the mth mode shape, and Fig. 23e presents the same value normalized as described in Eq. (27). The 7th most probable eigenvalue has the largest standard deviation. This corresponds to the higher CoV of the corresponding measured natural frequency (Table 2) and a significant error between the 7th most probable natural frequency and the corresponding measured value (Fig. 19d). Since the covariance matrix $\widetilde{\boldsymbol{\Sigma}}_{\lambda\phi\theta}(s_{\text{tol}})$ is not diagonal, meaning that the random variables λ, $\boldsymbol{\phi}$, and $\boldsymbol{\theta}$ are correlated, the standard deviation of the 6th eigenvalue, which is the second largest, can be associated with the relatively high NSDs of the most probable 6th mode shape and the 6th measured mode shape, as seen in Fig. 23e and Table 2. The standard deviation of the 3rd most probable eigenvalue corresponds to a higher CoV of the measured natural frequency (Table 2) and the large error of the 3rd numerical eigenvalue (Fig. 19d).

The estimated uncertainties of the most probable mode shapes are smaller than those of their measured counterparts. This is because the most probable modal parameters are estimated based not only on measurements but also on the structural insights that the FE model provides. However, the uncertainty of the most probable modal parameters may have been also artificially reduced due to the numerical regularization. The uncertainties can be affected by rejection of small singular values of $\mathbf{H}$ which reduces $\left\|\widetilde{\boldsymbol{\Sigma}}_{\lambda\phi\theta}(s_{\text{tol}})\right\|_{\text{F}}$ and thus also the parameter variances.

The variances and CoVs of the identified parameters θ_l are in agreement with those obtained through the mode matching method (Fig. 21), but they are higher. Similar to the uncertainties of the most probable modal parameters, the increased level of uncertainties of the connection parameters θ_l may be affected by the numerical regularization and the selected value of s_{tol}.

5. Computational efficiency in a larger-scale problem

The model updated in Section 4 using experimental data has 139 DOFs. This small-scale model properly reproduces structural modal data. However, in engineering practice larger-scale FE models are usually used. The number of iterations required to update a small-scale FE model may be not sufficient to assess the computational efficiency of the compared methods, which is a crucial aspect in case of a larger-scale FE model.

In this section both considered model updating methods are compared on a larger-scale FE model of a real four-bay lab frame described in detail in [25,37]. Despite the frame is not large itself, its FE model is designed to have a large number of DOFs, which is crucial to assess the computational effectiveness. The geometry of the model is shown in Fig. 24a. The structure consists of 11 beams connected via six couplers. All beams and couplers are the same. Each beam has the dimensions of $490 \times 80 \times 8$ mm. The structure is fixed at its ends. It is meshed using tetrahedral FEs with quadratic shape functions, as shown in Figs. 24b and c.

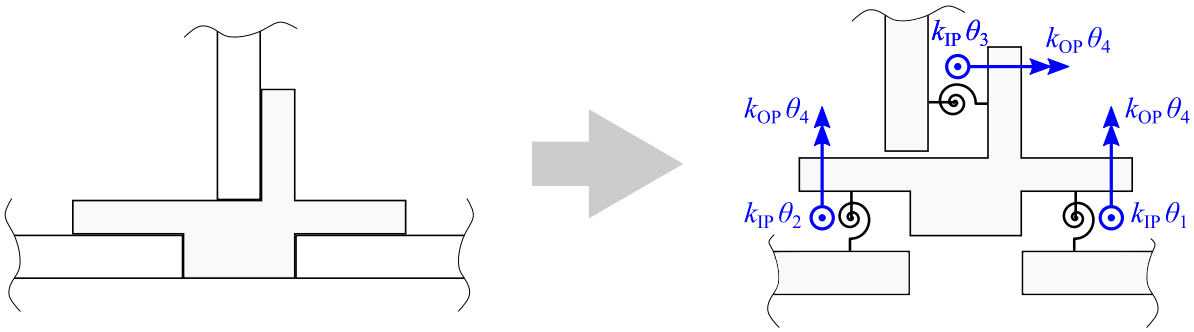

Fig. 25. Parameterization of the stiffness of bolted connections in the large-scale FE model. Rotation axes corresponding to the parameters are marked in blue.

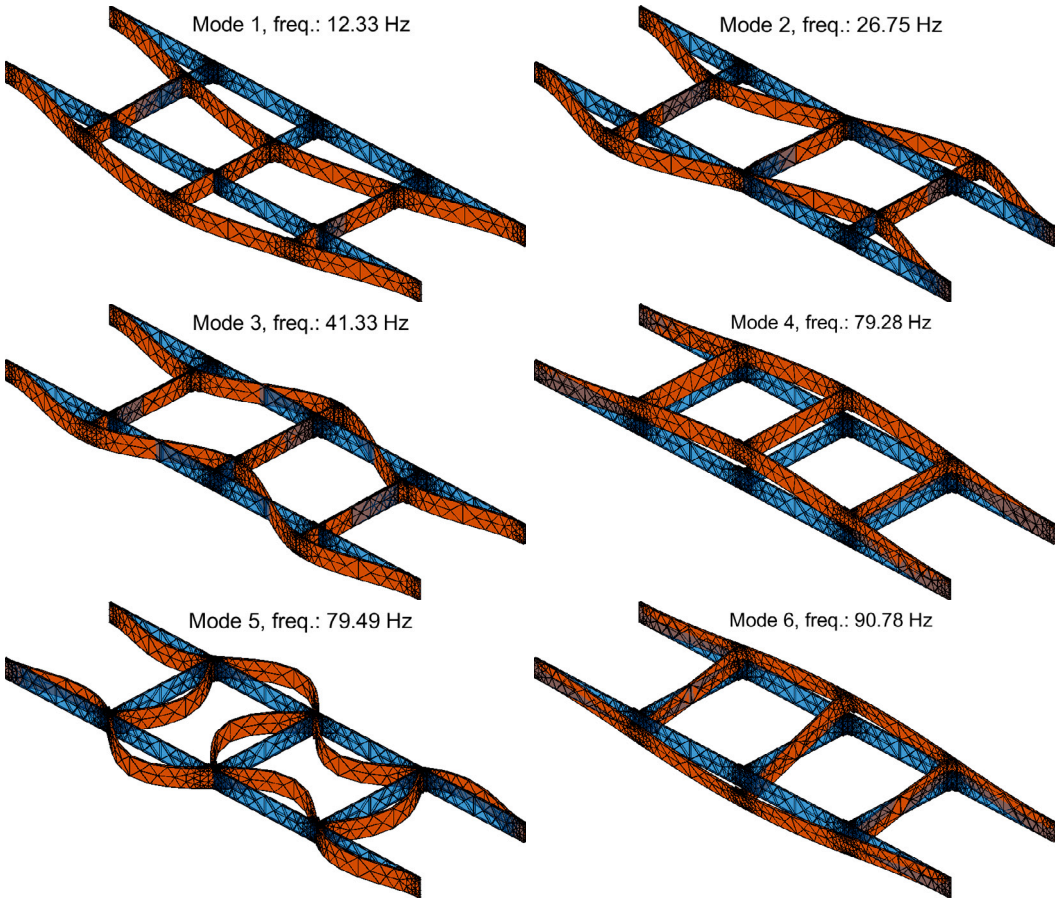

Fig. 26. Vibration modes obtained for the large-scale FE model parameterized by the exact values of the unknown parameters.

The geometry of the bolted connections between the beams and the couplers is simplified. Each bolted connection is represented by a pair of interfaces that are marked in Figs. 24b and c by distinctive colors. The FE nodes in each of these interfaces are constrained to move as a rigid body, so that their motion is represented by 6 DOFs. The corresponding interfaces are then assembled in such a manner that the three translational DOFs and the rotational DOF around the axis parallel to the beam are common. The remaining two rotational DOFs (with their rotation axes perpendicular to the beam) are connected via two rotational springs parameterized by two unknown parameters, as shown in Fig. 25. These parameters are common for all corresponding bolted connections between beams and couplers. In other words, the entire structure is parameterized with four unknown parameters, θ_1 to θ_4. The rotational stiffness constants k_{IP} (for in-plane rotation) and k_{OP} (for out-of-plane rotation) are equal to the bending stiffness of the beam connected to the coupler, multiplied by 50. This bending stiffness is calculated as the stiffness against the bending moment applied to the beam end, with the opposite end being fixed. The parameter θ_4, which is related to the out-of-plane rotation, is common

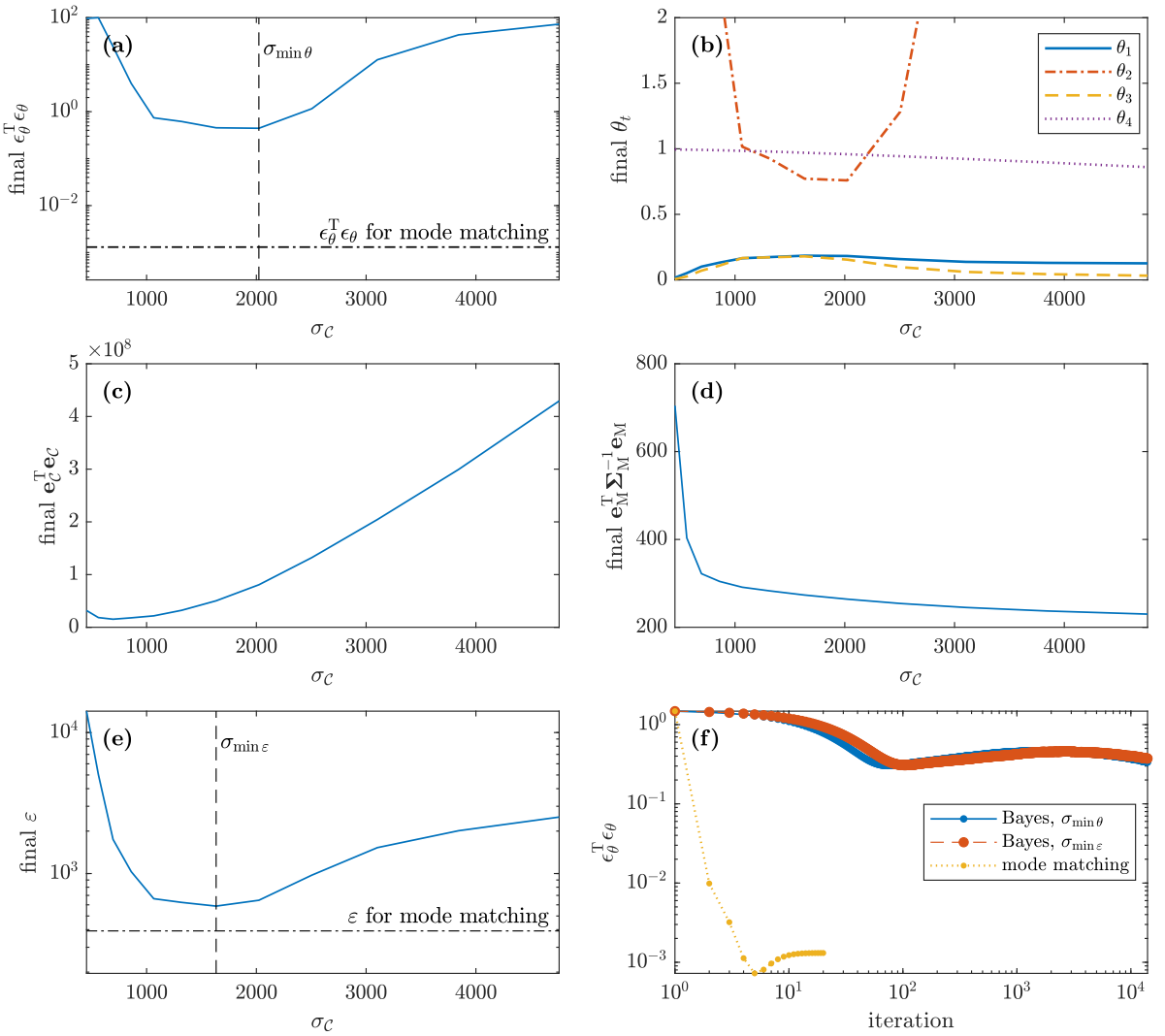

Fig. 27. Dependence of various error metrics obtained with the Bayesian approach on σ_C: (a) parameter estimate error together with the value obtained with the mode matching approach, (b) final values of the unknown parameters, (c) modeling error, (d) measurement error weighted by the reciprocal covariance matrix, (e) weighted norm of the differences between the numerical and measured modal data ε together with the value obtained with the mode updating approach, and (f) evolution of the parameter estimate error during the updating procedure for $\sigma_C = \sigma_{\min\theta}$, $\sigma_C = \sigma_{\min\varepsilon}$ together with the error obtained in the mode matching approach.

for all bolted connections, because an independent parameterization for all three bolted connections of the coupler would require high-frequency modes to estimate the parameters. Finally, the considered FE model has 31,848 DOFs.

Measured data are simulated using the described FE model. Sensor locations are selected as the mesh nodes closest to 1/3 and 2/3 of the beam length and placed in the middle of the beam width. There are 22 sensor locations, and each sensor records displacements in three directions (66 outputs total). The first six modes, depicted in Fig. 26, are used as the measurement data. They are obtained for the following values of the parameters: $\theta_1^{\text{exact}} = \theta_2^{\text{exact}} = \theta_3^{\text{exact}} = 0.36$ and $\theta_4^{\text{exact}} = 0.5$. These values are later treated as the exact values that are to be identified. To simulate measurement errors, Gaussian noise is added to the modal data. The eigenvalue noise is characterized by a 1% coefficient of variation, whereas the mode shape noise has the normalized standard deviation (NSD, Eq. (27)) of 5%. These values are similar as for the measured data listed in Table 2, and they are contained in the matrix $\boldsymbol{\Sigma}_M$ used in the Bayesian approach. The weighting matrix used for mode matching is its reciprocal.

The initial values of the unknown parameters used in model updating are: $\theta_{01} = \theta_{02} = \theta_{03} = \theta_{04} = 1$. In the Bayesian approach $\boldsymbol{\Sigma}_\theta = 10^{10}\mathbf{I}_{4\times4}$ is used. Mode matching is performed with the scaling factor $\kappa_\theta = 0.4$. For both methods the updating procedure is stopped when, for all unknown parameters, the following stop condition is satisfied: $\frac{|\Delta\theta_i|}{\theta_i} < 10^{-5}$.

The dependence of various error metrics on σ_C is shown in Fig. 27. To generate the plots 27a–e, the maximum number of iteration steps was limited to 3000, in order to finish the calculations in a reasonable time. The error vector $\boldsymbol{\epsilon}_\theta$ contains the differences between

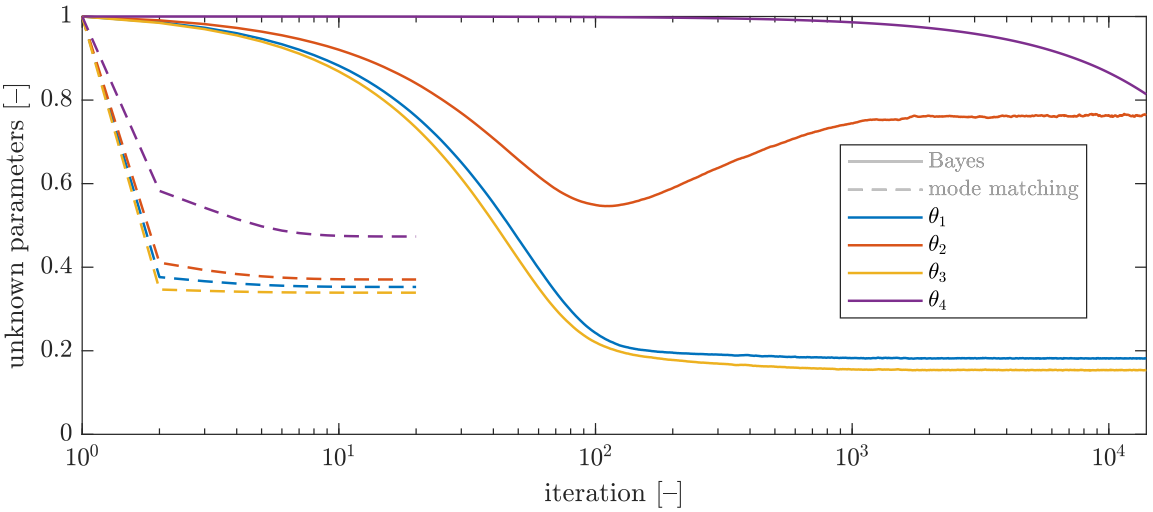

Fig. 28. Evolution of the unknown parameters for the Bayesian approach with $\sigma_C = \sigma_{\min\theta}$ and for the mode matching approach.

the current estimates of the unknown parameters and the corresponding exact values:

$$\boldsymbol{\epsilon}_\theta = \boldsymbol{\theta} - \boldsymbol{\theta}^{\text{exact}}. \tag{31}$$

Similarly to the previous analyses, both $\sigma_C = \sigma_{\min\theta}$ (Fig. 27a) and $\sigma_C = \sigma_{\min\varepsilon}$ (Fig. 27e) are used to establish the trade-off between the modeling error (Fig. 27c) and the measurement error (Fig. 27d).

The smallest parameter estimate error $\boldsymbol{\epsilon}_\theta^{\mathrm{T}}\boldsymbol{\epsilon}_\theta$ obtained with the Bayesian approach is significantly larger than that obtained by mode matching (Fig. 27a). It is due to the facts that the Bayesian approach requires more iteration steps than the maximum allowed number of 3000 (as shown in Figs. 27f and 28, where 14,000 iteration steps are allowed) and that the unknown parameters θ_1, θ_2, and θ_3 are strongly scattered around the exact value of 0.36. Mode matching yields results close to the exact values of the unknown parameters in 20 iteration steps only.

Despite the large dimensions of the mass and stiffness matrices, the time required for a single iteration step could be reduced to reasonable values of 7.6 s and 6.1 s for the mode matching and Bayesian approach, respectively. This time was achieved using a six-core Intel® Core™ i7-9750H processor with 32 GB RAM, a parallel implementation, and by exploiting the sparsity, symmetry, positive-definiteness, and the block structure of the involved matrices. The calculation time per iteration step is comparable for both methods, hence the number of iteration steps can be used as an indicator of the computational efficiency. In case of the Bayesian approach it is significantly larger than 14,000 (Fig. 28), while the mode matching requires only 20 steps.

6. Conclusions

In this study, two widely accepted methods for model updating, namely (1) the traditional mode matching method and (2) the Bayesian probabilistic framework based on the maximum a posteriori (MAP) formulation, were investigated, compared, and evaluated using a numerical examples and experimental data. The unknown parameters to be identified represented the stiffness of highly uncertain bolted connections in a frame structure. In the experimental study, the modal data of the structure were measured in a broadband frequency spectrum, including both lower-order modes and higher-order modes characterized by local curvatures. Such measurement data, and the high assembly discrepancies of the bolted connections revealed during the parametric identification, allowed to expose the pros and cons of both tested methods.

The Bayesian approach in both numerical and experimental studies required more iterations to update the FE model compared to the mode matching method. Tests on a large-scale FE model showed that both methods require a comparable computational time per single iteration step, but the Bayesian approach needed significantly more time to update the model due to the larger number of steps. To address numerical convergence problems, the experimental study required a two-stage model updating process, using first a simplified and then a fine parameterization. In the Bayesian approach, a challenge was to select the weighting parameter that represents expected model uncertainty, and it required several trial-and-error attempts. Both methods produced satisfactory and consistent values of the estimated parameters, provided the Bayesian approach was granted enough time to perform the required iterations. Only significant differences were noticed for the few stiffest bolted connections. For such stiff connections, modal characteristics of the frame structure are less sensitive to the stiffness parameters.

In estimating uncertainties, the Bayesian approach required numerical regularization using the TSVD, while the mode matching method did not encounter any numerical difficulties. The variances of the most probable modal parameters calculated through the Bayesian approach were smaller than the variances of the measured modal parameters, but variances of the unknown parameters

were slightly larger than those estimated through the mode matching method. The reason for this difference is not entirely clear: the calculation of the exact covariance matrix in the Bayesian approach was not possible, and it is difficult to determine if it is a result of a more reliable estimation or a side effect of the TSVD-based regularization. The estimated uncertainties of the unknown parameters generally agree with the differences between their values obtained through both tested methods.

Notwithstanding the described drawbacks, the Bayesian approach has an important advantage: it does not require matching between numerical and experimental modes. It is a valuable property, especially when mode matching is difficult due to a limited number of sensors. Despite its less sophisticated framework, the mode matching method provided more reliable results and was faster convergent. This suggests that it may be more suitable for practical applications, such as structural health monitoring, despite the similar final results. The limitations of the Bayesian approach may arise from the optimization procedure, which sequentially searches for the minimum of the objective function within three subspaces of the search space. In future research, it should be investigated whether the convergence and numerical stability of the method can be improved by refining the minimization algorithm.

CRediT authorship contribution statement

Mariusz Ostrowski: Conceptualization, Methodology, Software, Validation, Formal analysis, Investigation, Data curation, Writing – original draft, Writing – review & editing, Visualization. **Grzegorz Mikułowski:** Investigation, Resources, Writing – review & editing. **Bartlomiej Blachowski:** Conceptualization, Methodology, Writing – review & editing, Supervision. **Łukasz Jankowski:** Writing – review & editing, Supervision, Project administration, Founding acquisition.

Declaration of competing interest

The authors declare that they have no known competing financial interests or personal relationships that could have appeared to influence the work reported in this paper.

Data availability

Data will be made available on request.

Declaration of Generative AI and AI-assisted technologies in the writing process

During the preparation of this work the authors used ChatGPT and Google Translate in order to correct the grammar and punctuation of the text. After using these tools, the authors reviewed and edited the content as needed and take full responsibility for the content of publication.

Acknowledgments

The authors gratefully acknowledge the support of the National Science Centre, Poland granted through the project 2018/31/B/ST8/03152.

References

[1] M. Friswell, J.E. Mottershead, Finite element model updating in structural dynamics, Springer, Dordrecht, 1995, p. XII, 292, http://dx.doi.org/10.1007/978-94-015-8508-8.

[2] L. Gao, B. An, T. Xin, J. Wang, P. Wang, Measurement, analysis, and model updating based on the modal parameters of high-speed railway ballastless track, Measurement 161 (2020) 107891, http://dx.doi.org/10.1016/j.measurement.2020.107891.

[3] K.-V. Yuen, Bayesian Methods for Structural Dynamics and Civil Engineering, John Wiley & Sons, Ltd, 2010, pp. 11–98, http://dx.doi.org/10.1002/9780470824566.

[4] E. Simoen, G. De Roeck, G. Lombaert, Dealing with uncertainty in model updating for damage assessment: A review, Mech. Syst. Signal Process. 56–57 (2015) 123–149, http://dx.doi.org/10.1016/j.ymssp.2014.11.001.

[5] E. Simoen, C. Papadimitriou, G. Lombaert, On prediction error correlation in Bayesian model updating, J. Sound Vib. 332 (18) (2013) 4136–4152, http://dx.doi.org/10.1016/j.jsv.2013.03.019.

[6] Y. Yang, Y. Chen, A new direct method for updating structural models based on measured modal data, Eng. Struct. 31 (1) (2009) 32–42, http://dx.doi.org/10.1016/j.engstruct.2008.07.011.

[7] J.E. Mottershead, M. Link, M.I. Friswell, The sensitivity method in finite element model updating: A tutorial, Mech. Syst. Signal Process. 25 (2011) 2275–2296, http://dx.doi.org/10.1016/j.ymssp.2010.10.012.

[8] H. Sarmadi, A. Karamodin, A. Entezami, A new iterative model updating technique based on least squares minimal residual method using measured modal data, Appl. Math. Model. 40 (23) (2016) 10323–10341, http://dx.doi.org/10.1016/j.apm.2016.07.015.

[9] Y. Yuan, H. Liu, An iterative method for solving finite element model updating problems, Appl. Math. Model. 35 (2) (2011) 848–858, http://dx.doi.org/10.1016/j.apm.2010.07.040.

[10] J.D. Collins, J.P. Young, L.A. Kiefling, Methods and application of system identification in shock and vibration, in: System Identification of Vibrating Structures, 1972, pp. 45–71.

[11] J.D. Collins, G.C. Hart, T.K. Hasselman, B. Kennedy, Statistical identification of structures, AIAA J. 12 (2) (1974) 185–190, http://dx.doi.org/10.2514/3.49190.

[12] E. Zhang, P. Feissel, J. Antoni, A comprehensive Bayesian approach for model updating and quantification of modeling errors, Probab. Eng. Mech. 26 (4) (2011) 550–560, http://dx.doi.org/10.1016/j.probengmech.2011.07.001.

[13] M.B. Hermansen, J.J. Thomsen, Vibration-based estimation of beam boundary parameters, J. Sound Vib. 429 (2018) 287–304, http://dx.doi.org/10.1016/j.jsv.2018.05.016.
[14] M. Brøns, J.J. Thomsen, Vibration-based estimation of boundary stiffness and axial tension in beams using added mass, J. Sound Vib. 487 (2020) 115617, http://dx.doi.org/10.1016/j.jsv.2020.115617.
[15] M. Ostrowski, B. Blachowski, G. Mikułowski, Ł. Jankowski, Influence of noise in computer-vision-based measurements on parameter identification in structural dynamics, Sensors 23 (1) (2023) http://dx.doi.org/10.3390/s23010291.
[16] M. Ostrowski, B. Blachowski, B. Wójcik, M. Żarski, P. Tauzowski, Ł. Jankowski, A framework for computer vision-based health monitoring of a truss structure subjected to unknown excitations, Earthq. Eng. Eng. Vib. 22 (1) (2023) 1–17, http://dx.doi.org/10.1007/s11803-023-2154-3.
[17] Y. Zhang, Y. Zhao, H. Ouyang, Stochastic model updating for assembled structures with bolted joints using a Bayesian method, Eng. Optim. 54 (11) (2022) 1919–1931, http://dx.doi.org/10.1080/0305215X.2021.1965136.
[18] O. Sedehi, C. Papadimitriou, L.S. Katafygiotis, Probabilistic hierarchical Bayesian framework for time-domain model updating and robust predictions, Mech. Syst. Signal Process. 123 (2019) 648–673, http://dx.doi.org/10.1016/j.ymssp.2018.09.041.
[19] P. Van Overschee, B. De Moor, Subspace algorithms for the stochastic identification problem, in: Proceedings of the 30th IEEE Conference on Decision and Control, Vol. 2, 1991, pp. 1321–1326, http://dx.doi.org/10.1109/CDC.1991.261604.
[20] B. Peeters, System Identification and Damage Detection in Civil Engineering (Ph.D. thesis), 2000.
[21] J.-H. Yang, H.-F. Lam, An innovative Bayesian system identification method using autoregressive model, Mech. Syst. Signal Process. 133 (2019) 106289, http://dx.doi.org/10.1016/j.ymssp.2019.106289.
[22] T. Yin, X.-Y. Wang, H.-P. Zhu, A probabilistic approach for the detection of bolt loosening in periodically supported structures endowed with bolted flange joints, Mech. Syst. Signal Process. 128 (2019) 588–616, http://dx.doi.org/10.1016/j.ymssp.2019.04.010.
[23] K.-V. Yuen, J.L. Beck, L.S. Katafygiotis, Efficient model updating and health monitoring methodology using incomplete modal data without mode matching, Struct. Control Health Monit. 13 (1) (2006) 91–107, http://dx.doi.org/10.1002/stc.144.
[24] H. Sun, O. Büyüköztürk, Bayesian model updating using incomplete modal data without mode matching, in: T. Kundu (Ed.), Health Monitoring of Structural and Biological Systems 2016, Vol. 9805, SPIE, International Society for Optics and Photonics, 2016, pp. 108–116, http://dx.doi.org/10.1117/12.2219300.
[25] B. Blachowski, A. Świercz, P. Gutkiewicz, J. Szelążek, W. Gutkowski, Structural damage detectability using modal and ultrasonic approaches, Measurement 85 (2016) 210–221, http://dx.doi.org/10.1016/j.measurement.2016.02.033.
[26] B. Blachowski, Modal sensitivity based sensor placement for damage identification under sparsity constraint, Period. Polytech. Civ. Eng. 63 (2) (2019) 432–445, http://dx.doi.org/10.3311/PPci.13888.
[27] B. Blachowski, A. Świercz, M. Ostrowski, P. Tauzowski, P. Olaszek, Ł. Jankowski, Convex relaxation for efficient sensor layout optimization in large-scale structures subjected to moving loads, Comput.-Aided Civ. Infrastruct. Eng. 35 (10) (2020) 1085–1100, http://dx.doi.org/10.1111/mice.12553.
[28] S. Biswal, M.K. Chryssanthopoulos, Y. Wang, Condition identification of bolted connections using a virtual viscous damper, Struct. Health Monit. 21 (2) (2022) 731–752, http://dx.doi.org/10.1177/14759217211009217.
[29] F. Wang, Z. Chen, G. Song, Monitoring of multi-bolt connection looseness using entropy-based active sensing and genetic algorithm-based least square support vector machine, Mech. Syst. Signal Process. 136 (2020) 106507, http://dx.doi.org/10.1016/j.ymssp.2019.106507.
[30] K. Szopa, M. Iwaniec, J. Iwaniec, Modelling and identification of bolted truss structure with the use of design of experiment approach, Structures 27 (2020) 462–473, http://dx.doi.org/10.1016/j.istruc.2020.05.047.
[31] C. Li, Y. Jiang, R. Qiao, X. Miao, Modeling and parameters identification of the connection interface of bolted joints based on an improved micro-slip model, Mech. Syst. Signal Process. 153 (2021) 107514, http://dx.doi.org/10.1016/j.ymssp.2020.107514.
[32] M.S. Allen, D. Rixen, M. van der Seijs, P. Tiso, T. Abrahamsson, R.L. Mayes, Preliminaries: Primal and dual assembly of dynamic models, in: Substructuring in Engineering Dynamics: Emerging Numerical and Experimental Techniques, Springer International Publishing, Cham, 2020, pp. 5–24, http://dx.doi.org/10.1007/978-3-030-25532-9_2.
[33] J.V. Beck, K.J. Arnold, Parameter Estimation in Engineering and Science, John Wiley & Sons, 1977, http://dx.doi.org/10.1002/aic.690240233.
[34] A. Mróz, J. Holnicki-Szulc, K. Sekuła, Prestress Accumulation–Release (PAR) for damping of free vibrations in frame structures. Experimental study of a lab-scale demonstrator with piezo-actuated semi-active nodes, in: VIII ECCOMAS Thematic Conference on Smart Structures and Materials, (SMART 2017), 2017, pp. 145–156.
[35] B. Popławski, G. Mikułowski, R. Wiszowaty, Ł. Jankowski, Mitigation of forced vibrations by semi-active control of local transfer of moments, Mech. Syst. Signal Process. 157 (2021) 107733, http://dx.doi.org/10.1016/j.ymssp.2021.107733.
[36] M. Ostrowski, B. Blachowski, B. Popławski, D. Pisarski, G. Mikułowski, Ł. Jankowski, Semi-active modal control of structures with lockable joints: general methodology and applications, Struct. Control Health Monit. 28 (5) (2021) e2710, http://dx.doi.org/10.1002/stc.2710.
[37] B. Blachowski, A. Świercz, N. Pnevmatikos, Experimental verification of damage location techniques for frame structures assembled using bolted connections, in: 5th International Conference on Computational Methods in Structural Dynamics and Earthquake Engineering, (COMPDYN 2015), 2015, pp. 2588–2599, http://dx.doi.org/10.7712/120115.3561.1511.